

Improved Tumor Discrimination and Shortened Administration-to-Imaging Times in Fluorescence Guided Surgery Through Paired-Agent Protocols

Cheng Wang

Dartmouth College

Margaret Folaron

Dartmouth College

Jason Gunn

Dartmouth College

Sassan Hodge

Dartmouth College

Eunice Chen

Dartmouth College

P. Jack Hoopes

Dartmouth College

Kenneth Tichauer

Illinois Institute of Technology

Kimberley Samkoe (✉ Kimberley.S.Samkoe@dartmouth.edu)

Dartmouth College

Research

Keywords: Paired-agent imaging, fluorescence guided surgery, Head and neck squamous cell carcinoma, ep-idermal growth factor receptor, ABY-029, IRDye 700DX

Posted Date: November 20th, 2020

DOI: <https://doi.org/10.21203/rs.3.rs-111011/v1>

License: © ⓘ This work is licensed under a Creative Commons Attribution 4.0 International License.

[Read Full License](#)

1 **Improved tumor discrimination and shortened administration-to-imaging times in fluores-**
2 **cence guided surgery through paired-agent protocols**

3

4 Cheng Wang,¹ Margaret Folaron,¹ Jason R. Gunn,¹ Sassan Hodge,² Eunice Y. Chen,^{2,3} P. Jack
5 Hoopes,^{1,2,3} Kenneth M. Tichauer,⁴ Kimberley S. Samkoe^{1,2,3*}

6

7 1. Thayer School of Engineering, Dartmouth College, Hanover, NH

8 2. Department of Surgery, Dartmouth-Hitchcock Medical Center, Lebanon, NH

9 3. Geisel School of Medicine, Dartmouth College, Hanover, NH

10 4. Biomedical Engineering, Illinois Institute of Technology, Chicago, IL

11

12 *Corresponding Author: Kimberley S. Samkoe, Kimberley.S.Samkoe@dartmouth.edu, phone:
13 603-650-7618

14

15

16

17 **Abstract**

18 **Background:** The goal of fluorescence guided surgery (FGS) in oncology is to improve the sur-
19 gical therapeutic index by enhancing contrast between cancerous and healthy tissue. However,
20 optimal discrimination between these tissues is complicated by the non-specific uptake and reten-
21 tion of molecular targeted agents and the heterogeneity of fluorescence signal. Paired-agent imag-
22 ing (PAI) employs co-administration of an untargeted imaging agent with a molecular targeted
23 agent, providing a normalization factor to minimize nonspecific and heterogeneous signals. The
24 resulting measured binding potential is quantitative and equivalent to *in vivo* immunohistochem-
25 istry of the target protein. This study demonstrates that PAI improves the accuracy of tumor-to-
26 healthy tissue discrimination compared to single agent imaging for *in vivo* FGS.

27 **Methods:** PAI using a fluorescent anti-EGFR affibody molecule (ABY-029, eIND 122681) with
28 untargeted IRDye 700DX carboxylate was compared to ABY-029 alone in an oral squamous cell
29 carcinoma xenograft mouse model at 3 hours ($n = 30$).

30 **Results:** PAI significantly enhanced tumor discrimination, as compared to ABY-029 alone (diag-
31 nostic accuracy - 0.94 vs 0.86, ROC curve AUC - 0.991 vs. 0.925, respectively). Additionally, the
32 AUC of the ROC curve for PAI was stable as patient cohort number was increased from $n = 1$ to
33 20, while ABY-029 decreased as n increased, indicating a potential for universal FGS image
34 thresholds to determine surgical margins. In addition, PAI reduced the administration-to-imaging
35 time from 3 hours to 30 minutes and exhibited a statistically stronger correlation to EGFR expres-
36 sion heterogeneity ($r = 0.58$ compared to $r = 0.47$, $p = 9 \times 10^{-8}$).

37 **Conclusion:** The quantitative receptor delineation of PAI promises to improve the surgical thera-
38 peutic index of cancer resection in a clinically relevant timeline.

39

40 **Keywords:** Paired-agent imaging, fluorescence guided surgery, Head and neck squamous cell car-
41 cinoma, epidermal growth factor receptor, ABY-029, IRDye 700DX

42

43

44 **Background**

45 Completeness of surgical resection is a critical determinant for the survival of patients with head
46 and neck cancers. Residual tumor increases tumor-related death at 5-years by 90% compared to
47 those with truly negative margins (1) but the use of wide margins to remove residual tumor can
48 lead to severe morbidity. The near ubiquitous overexpression of epidermal growth factor receptor
49 (EGFR) - with estimates of > 90% overexpression in SCC (2,3) - has led to the development of
50 numerous molecular therapeutic agents, which have been subsequently leveraged for fluorescence
51 imaging (4–8). The goal of molecular-targeted fluorescence-guided surgery (FGS) is to improve
52 the surgical therapeutic index based on the overexpression of the molecular target in tumor com-
53 pared to normal tissue. Several studies have reported advantages of FGS for identifying bulk tumor
54 and tumor margins using therapeutic antibodies (cetuximab, panitumumab) labeled with IRDye
55 800CW (LI-COR Biosciences, Inc.) (7,9–11). However, true molecular contrast using FGS is con-
56 founded by heterogeneous uptake and nonspecific retention of targeted imaging agents within all
57 tissue types. Paired-agent imaging (PAI) methods have the potential to overcome these confound-
58 ing effects through co-administration of a second, untargeted, control fluorescent agent enabling
59 imaging of the receptor concentration, rather than agent concentration. This pre-clinical project
60 compares the accuracy of tumor discrimination using conventional “single-agent imaging” (SAI)
61 and the proposed PAI in an orthotopic xenograft mouse model of human head and neck cancer.

62 In recent years, FGS has been improved by two advancements: the aforementioned PAI
63 and the development of an anti-EGFR fluorescent Affibody molecule (ABY-029). PAI, which
64 reports the “binding potential” (BP, a value proportional to receptor concentration), has been used
65 in a variety of EGFR-overexpressing xenograft cell lines to demonstrate that tumor-averaged bind-
66 ing potential scales linearly with EGFR both *in vivo* and *ex vivo* (12). This *in vivo* phenomena was

67 linearly correlated with *ex vivo* tumor EGFR immunohistochemistry (13) and shown to non-inva-
68 sively detect fewer than 200 tumor cells in draining lymph nodes (14). However, the ability of PAI
69 to truly improve tumor discrimination in FGS has never been quantitatively assessed.

70 ABY-029 was developed to decrease administration-to-imaging time (hours instead of
71 days) and reduce immunogenicity compared to antibody imaging agents (6). ABY-029 is currently
72 being tested in Phase 0 studies in a number of solid tumor types, including head and neck cancers.
73 In the work presented here, we utilize two orthotopic SCC base of tongue tumors (FaDu and De-
74 troit 562) and a highly expressing EGFR SCC of the skin (A431) to compare the accuracy and
75 efficiency of FGS tumor resection using ABY-029 alone versus PAI with ABY-029 in combina-
76 tion with control IRDye 700DX carboxylate.

77

78

79 **Methods**

80 *Cell lines and culture methods*

81 Human squamous cell carcinoma cell lines used in this study included FaDu, a pharynx carcinoma,
82 Detroit 562, a metastatic pharynx carcinoma derived from pleural effusion, and A431, an epider-
83 mal SCC. All three cell lines were purchased from the ATCC (Manassas, VA, USA) and were
84 cultured according to ATCC specifications with the addition of 1% penicillin-streptomycin.

85

86 *Imaging agents*

87 ABY-029 was obtained from the University of Alabama at Birmingham (UAB) Vector Production
88 Facility and manufactured under Good Laboratory Practice (GLP) as previously described (6). The
89 ABY-029 human microdose is defined as 30 nanomole per human, (3.96 $\mu\text{g}/\text{kg}$ for a 60 kg human).

90 Using the method of Reagan-Shaw (2007)(15), the mouse-equivalent dose was determined to be
91 48.8 $\mu\text{g}/\text{kg}$ for an average 22 g mouse, for a final dose of 1.07 $\mu\text{g}/\text{mouse}$. IRDye 700DX NHS
92 ester was purchased from LI-COR Biosciences, Inc. (Lincoln, NE) and converted to carboxylate
93 form by dissolving in PBS (pH = 8.5) and stirring at room temperature for 5 hours.

94

95 *Mouse xenograft model*

96 All animal procedures were approved by the Dartmouth Institutional Animal Care and Use Com-
97 mittee (IACUC) and conducted according to NIH-OLAW and AAAALAC guidelines. Female,
98 athymic nude mice, 6-8 weeks of age, were purchased from Charles River Laboratories (Wilmington,
99 MA). Tongue tumors were implanted using a 25-gauge needle and 5×10^5 cells in 50 μL cul-
100 ture medium. Ten mice were implanted per cell line ($n_{\text{total}} = 30$). PAI was performed on six mice
101 for FaDu, and seven each for Det 562 and A431 tumor lines, and the remaining mice were used
102 for auto-fluorescence imaging. An additional 30 mice were implanted with FaDu for the admin-
103 istration-to-imaging time study ($n = 5$ mice/time point). Tumor take was 100% and were used for
104 imaging when the diameter reached $\sim 3\text{-}4$ mm.

105

106 *ABY-029 and IRDye 700DX fluorescence imaging*

107 Mice were administered 200 μL of a 1:10 molar ratio of 0.68 μM ABY-029 and 6.8 μM IRDye
108 700DX in sterile phosphate buffered saline (PBS) via intravascular tail vein injection (Fig 1A).
109 Injection concentrations were determined by assessing fluorescence signal at three hours compared
110 to non-injected autofluorescence of the tissue (*Supplemental Data, Section S1*). The mice were
111 sacrificed by cervical dislocation while anesthetized to a surgical plane (1.5-2% isoflurane, 1

112 L/min O₂) 3-hours post-administration, with the exception of the time study where sacrifice oc-
113 curred at 0.25, 0.5, 1, 2, and 5 hours. Note that the 3-hour FaDu tumors were also used in the time
114 study to minimize animal use. The tongue was excised at the base, bisected along the raphe, and
115 placed on a glass slide cut-face down. A section of normal leg muscle (EGFR-negative control)
116 was also included. *Ex vivo* images of the tissues were collected for both ABY-029 and IRDye
117 700DX carboxylate on the Odyssey CLx (LI-COR Biosciences, Inc.) using the following settings:
118 auto function for laser intensity, 1-mm focus offset, medium quality, and 42- μ m resolution.

119

120 *PAI binding potential map creation*

121 PAI binding potential (*BP*) maps were calculated from of the ABY-029 and IRDye 700DX images
122 using the single-time point (STP) method (Equation 1), first described by Tichauer et al (16) (Fig
123 1B). Note that in this previous work, pre-injection images were subtracted from the post-injection
124 image to remove the contribution of autofluorescence. Pre-administration images were not sub-
125 tracted and autofluorescence contribution is discussed in the *Supplemental Data, Section S1*. For
126 each pixel within the image, the BP was calculated using

$$127 \quad BP = \frac{I_T}{I_U \times NF} - 1 \quad (1)$$

128 where I_T and I_U are the pixel intensity of the targeted (ABY-029) and untargeted (IRDye 700DX)
129 imaging agents, respectively, and NF is the normalization factor determined by Equation 2.

$$130 \quad NF = (BP_{norm} + 1) \frac{\bar{I}_{T(norm)}}{\bar{I}_{U(norm)}} = \frac{1.5 \bar{I}_{T(norm)}}{\bar{I}_{U(norm)}} \quad (2)$$

131 where $\bar{I}_{T(norm)}$ and $\bar{I}_{U(norm)}$ are the mean pixel intensities of the targeted and untargeted imaging
132 agents, respectively, in the normal tongue. The NF is calculated independently for every ABY-029
133 and IRDye 700DX image pair. The BP_{norm} is the binding potential of the normal tongue, which
134 was artificially set to 0.5 in order to have a “near-zero” BP value in the normal tongue tissue while

135 avoiding negative pixels. The selection of the *NF* is described in detail in the *Supplemental Data*,
136 *Section S2*, where it is demonstrated that the selection of the *NF* does not alter the observed contrast.

137

138 *Pathology*

139 After imaging, the tongue sections were placed on filter paper to maintain orientation and fixed in
140 10% buffered formalin (Biochemical Science, Inc) in histological cassettes. Standard H&E and
141 EGFR immunohistochemistry (IHC) staining were performed by the Norris Cotton Cancer Center
142 Pathology Translational Research Resource as described previously (13). RGB images of whole
143 H&E and EGFR IHC tissue sections were collected on the Vectra 3 (Perkin Elmer) at 4X magni-
144 fication. The stitched overview image was saved as an RGB three image stack .tiff file, then con-
145 verted to a single .tiff file using the concatenate arrays function (*cat*) in MATLAB version R_2017a.

146

147 *Image Preparation and Co-registration*

148 Five image types are used for in this study: H&E, EGFR IHC, ABY-029, IRDye 700DX,
149 and BP maps. Prior to alignment and co-registration, several steps were taken to prepare the images.
150 ABY-029, IRDye 700DX and BP maps were inherently co-registered as a function of imaging on
151 the Odyssey CLx (42 $\mu\text{m}/\text{pixel}$). The H&E and EGFR IHC images collected on the Vectra scanner
152 (1 $\mu\text{m}/\text{pixel}$) were resized to match the fluorescent images. The brown stain indicating EGFR in
153 the IHC images was isolated by using the H DAB Color Deconvolution script in FIJI (17) and then
154 normalized to the average stain intensity in the placenta positive control slide for each staining
155 batch to correct for variations in stain intensity due to color development. Image alignment and
156 co-registration of the fresh tissue sections with pathology was performed using a previously de-
157 scribed procedure (18). Briefly, the BP map was co-registered to the EGFR IHC image using

158 *warp_it* in MATLAB that utilizes point set registration and point matching to spatially transform
159 and align the images. Visualization of the overlaid images is provided in the *Supplemental Data*,
160 *Section S3*. The H&E were not used for image analysis, and thus the coordinate transformation
161 determined for the IHC was applied to the H&E image for visualization purposes only.

162

163 *Image Analysis and Statistics*

164 For each sample, a pathologist drew regions-of-interest (ROI) for normal tongue muscle, tumor,
165 and salivary gland using EGFR IHC, which were manually converted and translated to co-regis-
166 tered fluorescence and BP images for both mean and pixel-by-pixel analysis of tissue type. The
167 visualization of ABY-029, IRDye 700, and BP are presented by “fire,” “kryptonite,” and “ice”
168 pseudo colormaps as defined by *COLORMAP* (<https://jdherman.github.io/colormap/>). Histograms
169 were created in OriginPro 2018 (OriginLab). Receiver operating characteristic (ROC) curves were
170 calculated with either *perfcurve* function in Matlab, or ROC analysis in OriginPro. Statistically
171 significant differences in group means were analyzed in OriginPro with a one-way ANOVA with
172 Bonferroni correction to avoid Type I error. Diagnostic parameters, including area under the-curve
173 (AUC), sensitivity, specificity, positive prediction value (PPV), negative prediction value (NPV),
174 and diagnostic accuracy were determined. To study the correlation of EGFR heterogeneity, pixel
175 intensity values were extracted from deconvoluted IHC images, fluorescent images, and BP maps
176 and were normalized to the highest pixel value. To study the impact of image resolution on the
177 correlation of EGFR staining and fluorescent images, *imagepyramid* in Matlab was used for aver-
178 aging four adjacent pixel values. Pixel-by-pixel correlation was performed using Pearson product
179 correlation (r) in OriginPro. Contrast-to-Variance Ratio (CVR) was defined by:

$$180 \quad CVR = \frac{\mu(I_T) - \mu(I_N)}{\sqrt{\sigma_T^2 + \sigma_N^2}} \quad (3)$$

181 $\mu(I_T)$ and $\mu(I_N)$ represent mean fluorescence or BP, and σ_T and σ_N represent the standard deviation of fluorescence or BP values in tumor and normal tissue, respectively. Statistical significance of BP and fluorescence intensity over time was calculated using one-way repeated measures ANOVA.

185

186 **Results**

187 *Administration dose and the normalization factor*

188 In previous studies (13,14), a pre-injection background image was used to remove the absolute tissue autofluorescence signal on a pixel-by-pixel basis; however, in this study and during FGS process, pre-injection images within the excised tissue and surgical wound bed are not available. This had two effects on study design. First, autofluorescence was used to determine the appropriate administered paired-agent dose. A 1:10 molar ratio of ABY-029:IRDye 700DX was used in order to obtain fluorescence signal ~8 times the autofluorescence at 3 hours (see *Supplemental Figure S1 & S2*). Second, the normalization factor (NF) was determined at each time point by setting the BP equal to 0.5 by using the average ABY-029 and IRDye 700DX fluorescence signal in normal tongue, rather than using EGFR-devoid leg muscle in the first post-administration image. CVR (Equation 3) was used to standardize the measurements and compare image contrast between PAI and SAI as tumor-to-background ratios (TBR) were found to be unstable (see *Supplemental Figure S3*).

200

201 *Discrimination of tumor and normal tissue*

202 To evaluate the ability of PAI and SAI to distinguish tissue types based on signal alone, we analyzed the resultant images in two ways: region of interest (ROI) averages and region pixel-to-pixel

204 comparisons. After co-registration, the fluorescence intensity of ABY-029 and the BP were com-
205 pared for tumor (FaDu, Detroit 562 and A431), normal tongue, salivary gland if present, and leg
206 muscle (negative control, Fig. 2A). A representative example of ABY-029 targeted fluorescence
207 intensity and BP is plotted in Fig. 2B to demonstrate the variability of the signal in each tissue.
208 The ROI-specific averages for each tissue type are shown in increasing order of EGFR expression
209 (Fig. 2C). A one-way ANOVA analysis with Bonferroni correction demonstrated that all fluores-
210 cence means were not the same for ABY-029 fluorescence ($p < 9 \times 10^{-26}$) or BP ($p < 2 \times 10^{-23}$). The
211 Bonferroni individual means comparison showed the ABY-029 fluorescence of Detroit 562 and
212 A431 tumors were significantly different from all normal tissues, while FaDu, salivary gland, and
213 normal tongue were not significantly different from each other. Leg muscle, which lacks EGFR
214 expression, has significantly lower ABY-029 fluorescence compared to all other tissues. Individ-
215 ual means comparison for BP showed that all tumor lines were significantly different from all
216 normal tissues, all normal tissues were significantly different from each other, but FaDu and De-
217 troit 562 could not be statistically distinguished.

218 Although tumor and normal tissues could be identified based on BP means, the histograms
219 in Fig. 2B demonstrate a substantial overlap in the distribution of pixel values between some
220 groups. Therefore, tissue type comparison of SAI and PAI was performed on the co-registered
221 images on a pixel-to-pixel basis (Fig. 3). Representative co-registered IRDye 700DX fluorescence,
222 ABY-029 fluorescence, and BP map images are shown for each tumor line with pathological im-
223 ages (Fig. 3A). Co-registered pixel intensities from the EGFR IHC (gold standard) and fluores-
224 cence images were used to plot receiver-operating characteristic (ROC) curves to evaluate the di-
225 agnostic ability of both SAI and PAI. For each tumor type, BP maps yielded higher area-under-the
226 curve (AUC) values than either ABY-029 and IRDye 700DX alone. When mice were grouped into

227 cohorts of individual tumor type and all tumor lines (Fig. 3B), the BP AUCs were ≥ 0.990 , while
228 ABY-029 AUCs were consistently lower. The cohort diagnostic accuracy statistics are summa-
229 rized in Fig. 3B, with the higher value highlighted in green for ease of interpretation. BP maps
230 demonstrated statistically higher ($p < 0.05$) diagnostic ability in all cases, with the exception of
231 Detroit 562, in terms of sensitivity and negative predictive value (NPV).

232

233 *Representation of tissue heterogeneity*

234 EGFR expression within tumors was highly heterogeneous, especially compared to normal tissues,
235 as can be observed in the IHC images (Figs. 2 and 3). Heterogeneous EGFR expression can con-
236 tribute to difficulties in distinguishing tissues; therefore, we assessed the pixel-by-pixel linear cor-
237 relation between IHC stain intensity with BP, and ABY-029 and IRDye 700DX fluorescence (Fig.
238 4). To assess the effects of co-registration error on the high resolution ($42 \mu\text{m}/\text{pixel}$) images, an
239 image pyramid algorithm (Fig. 4A) was used to incrementally decrease resolution. The resulting
240 scatter plots, and the corresponding Pearson coefficients (r) for each resolution tested in a repre-
241 sentative FaDu tumor are shown in Fig. 4A. At Level 0 ($42 \mu\text{m}/\text{pixel}$), all three image types ex-
242 hibited a moderate correlation with IHC with BP demonstrating the strongest correlation while the
243 non-targeted IRDye 700DX is negatively correlated. As image resolution is decreased, the strength
244 of the correlation between EGFR IHC and all three image types non-targeted IRDye 700DX is
245 negatively correlated increase, with BP maintaining the strongest correlation at each level. The
246 correlation between the IHC and IRDye 700DX was negative and remained low (0.1-0.3) to mod-
247 erate (0.3-0.5); therefore, only the correlations between IHC and BP or targeted fluorescence were
248 further analyzed. The rate of change in r is plotted in Fig. 4B and plateaued after a 1/8 reduction
249 in resolution. Clinical imaging systems (wide-field to endoscopic) have spatial resolution of 50-

250 500 μm (grey shaded region, Fig. 4B).(19) Therefore, a 1/4 reduction in the original resolution
251 (168 μm), was applied in further analyses of each tumor group. Overall, the Pearson coefficients
252 were 0.58 ± 0.04 and 0.47 ± 0.05 for BP and ABY-029, respectively ($p < 0.0001$). In all cases,
253 IHC demonstrated a stronger correlation with BP than ABY-029 fluorescence alone ($p < 0.005$).

254

255 *Reduction of administration-to-imaging time*

256 To maximize observed FGS contrast, the delay time between agent administration and surgery
257 must be optimized. To study administration-to-imaging time of PAI, mice ($n = 5$ or 6 per group)
258 were co-administered ABY-029 and IRDye 700DX, then sacrificed at varying time points up to
259 5 hours after administration (Fig. 5). Representative SAI and PAI images for a single animal at
260 each time point, as well as plots of the average signal intensity in the tumor region over all times
261 are shown (Fig. 5A). The ability to distinguish the tumor region improved with time after injec-
262 tion for both SAI and PAI. The PAI BP yielded a stable CVR of 2.0 ± 0.2 by 30 min post-agent-
263 injection, while ABY-029 alone required 3 h to reach a CVR plateau of only 2.2 ± 0.3 (Fig. 5B).
264 PAI BP demonstrated a higher CVR compared to ABY-029 SAI at all time points (Fig. 5B);
265 however, they are only significantly different during the first 2 hours determined by One-Way
266 repeated measures ANOVA with time as a within-subjects variable ($p < 0.05$). ROC curves for
267 BP and ABY-029 were plotted for each time point (Fig. 5C). The AUCs of both BP and ABY-
268 029 alone increase over time; however, at each time point the PAI BP AUCs are higher than SAI
269 AUCs. Moreover, SAI AUC increases over the 5-hour administration-to-imaging time with no
270 demonstration of stabilization.

271

272 **Discussion**

273 Molecular PAI protocols have been proven to provide significant advantages for estimating
274 true molecular contrast and for enabling unmatched specificity and sensitivity (13,14). As previ-
275 ously demonstrated (16,20), the tissue-averaged PAI binding potential (BP) in this work scaled
276 with EGFR expression in tumor lines, and the means of all tumor lines studied were significantly
277 higher compared to all normal tissues (Fig 2). In comparison, the mean fluorescence intensity from
278 SAI with ABY-029 alone failed to be able to separate the lowest EGFR expressing tumor line from
279 normal oral tissues. However, the broad heterogeneity of both BP and fluorescence intensity in
280 PAI and SAI, respectively, warranted further investigation of the diagnostic abilities of these meth-
281 odologies (Fig 2B). Therefore, studies mimicking in-patient and back-table intraoperative assess-
282 ment strategies (2) were undertaken to compare PAI and SAI to gold standard H&E and EGFR
283 immune-stained formalin-fixed paraffin embedded pathological specimens, with co-registration to
284 PAI and SAI and correlation on a pixel-to-pixel basis (Fig 3).

285 In every category tested, including ROC curve determined AUC and diagnostic tests (Fig
286 3), PAI outperformed SAI with the exception of sensitivity and negative predictive value (NPV)
287 for the Detroit 562 cell line (Fig 3B). Both sensitivity and NPV include “False Negatives” in the
288 denominator, suggesting that Detroit 562 had a high number of pixels within the pathologist-des-
289 ignated tumor regions that were classified as normal tissue based on PAI as compared to SAI. This
290 discrepancy can be explained by the fact that the “pathologist-determined tumor” contains regions
291 of low-EGFR expressing tissue (Fig. 2B), and PAI is designed to enhance contrast as a function
292 of targeted molecule (in this case, EGFR expression). When considering the whole tumor on a
293 pixel-to-pixel basis, the regions devoid of EGFR decreased the measured predictive power of PAI
294 because it is truly a molecular signal, unlike SAI that is a mixture of molecular targeted and non-
295 specific signal from the enhanced permeability and retention (EPR) effect. In cases where EGFR

296 expression is low or there are large non-EGFR staining regions within the tumor, SAI may be able
297 to better differentiate tumor from normal tissue based on EPR effect. Data in soft-tissue sarcomas
298 that suggests this is the case by demonstrating that overall tumor contrast was enhanced and fluo-
299 rescent signal heterogeneity minimized by simultaneously imaging perfusion-based ICG accumu-
300 lation with ABY-029 in a single imaging channel (21,22). However, perfusion agents may be better
301 for this capacity. Further investigation is required in tumors with large negative regions, or with
302 lower cellular density—often seen in aggressive cell lines commonly used for xenograft models
303 (due to fast growth rate), yet not necessarily indicative of patient population tumor characteristics.

304 It is interesting to note, as we moved from ROC analysis of a single animal ($n = 1$ per cell
305 line, Fig. 3A) to a tumor cohort ($n = 6$ or 7 per cell line, Fig 3B) and finally, to all tumor cohort (n
306 $= 20$, Fig 3B) that the AUC of BP remained relatively constant ($AUC \geq 0.99$) while the AUC of
307 ABY-029 fluorescence decreased as the group size increased. This is important when considering
308 broad implementation of FGS into surgical suites. Fluorescence intensity alone can vary widely
309 patient-to-patient, owing to variability in fluorescent agent administration, delivery, and excretion,
310 which increased variability causing the sensitivity and specificity to decrease as the sample size
311 increases. The stability of PAI AUC of the ROC over increasing patient populations was likely
312 due to PAI ratio-metric imaging methodologies removing the hemodynamic variation of delivery
313 and clearance rates of the dye between individuals. BP calculated using PAI could be a promising
314 standard threshold for tumor region detection, a hypothesis that will be explored in future planned
315 clinical studies.

316 Tumor spatial heterogeneity is an important prognostic factor, and accurately imaging re-
317 ceptor expression heterogeneity is key for identifying tumor regions. This is especially important
318 when attempting to identify tumor in the surgical margins where cell density, and therefore EGFR

319 concentrations, may be low. As anticipated from previous studies, PAI and ABY-029 were posi-
320 tively correlated, while untargeted IRDye 700DX was negatively correlated with EGFR IHC (Fig
321 4B) (21). At 42- μ m resolution, ABY-029 and PAI BP were only moderately correlated with gold
322 standard IHC images (Fig 4B). This may be due to several factors. First, it can be observed that
323 there is a large population of pixels in the IHC images that were clustered at the highest measurable
324 pixel values (Fig 4B) due to the limited dynamic range of IHC images (0~2 OD). All three tumor
325 lines had intense IHC staining and have been found to have moderate to high EGFR expression
326 ($1.2 (\pm 0.3) \times 10^6$, $1.6 (\pm 0.6) \times 10^5$, and $7.4 (\pm 0.4) \times 10^4$ EGFR receptors/cell in A431, Detroit 562,
327 and FaDu, respectively; see *Supplemental Table S1 & Fig S5*) and received a pathologist score of
328 3+ with strong, continuous membranous staining. Secondly, the imperfect registration between
329 fresh tissue fluorescence images and fixed pathological tissue images could substantially reduce
330 correlation, especially at high image resolutions where single pixel misalignments are likely. This
331 was validated when lower, but still clinically viable, image resolutions were examined using a 4 \times 4
332 Gaussian filter and improvements in correlations for both PAI and ABY-029 SAI were observed
333 (Fig 4). This indicates that better methodologies for spatial correlation of fresh tissue to patholog-
334 ically stained sections are needed for single cell assessment of surgical margins.

335 Image contrast-to-variance between the tumor and the normal tissue depends on many fac-
336 tors, including the administration-to-image timing (to allow normal tissue clearance), the instru-
337 mentation used, the dose of fluorophore given, the health of the patient (e.g., diseased liver/kidney
338 may extend plasma half-life), the physiology of the tumor and healthy tissue (e.g., blood flow and
339 vascular permeability), the on- and off- rate constants of specific agent binding, the level of non-
340 specific agent binding, and volume of tissue interrogated. *In situ* imaging, where decision making
341 may be most critical, tends to exhibit lower image contrast-to-variance than excised tissues(23),

342 likely attributable to the nonspecific signal arising from the bulk normal tissue. There have been
343 many strategies tested to increase contrast by decreasing non-specific signal. Administration of a
344 pre-dose, or “cold dose”, of a non-fluorescent antibody an hour prior to a fluorescent antibody has
345 been used to decrease contribution of molecular target sinks within the body. However, the results
346 for these studies have been mixed. Moore *et al.*(24) and Voskuil *et al.* (7) demonstrated improved
347 tumor-to-background ratios by pre-dosing whereas Nishio *et al.* (25) concluded that there was no
348 additional value added.

349 A large body of work, including clinical trials, has been produced using high-dose ICG and
350 “second window” administration-to-imaging times (AIT) i.e., 24 h AIT. The high dose of ICG
351 allows sufficient tumor accumulation such that the tumor is visible at 24 hours, even with the fast
352 plasma and normal tissue clearance typically observed. In addition, several groups have demon-
353 strated the use of IRDye 800CW labeled EGFR-targeted antibodies with surgery and imaging at
354 1-4 days post-administration (4,5,24,25), with optimum fluorescence intensities observed within
355 the first 2 days (25). On the other hand, ABY-029 (~8 kDa)—with its considerably faster plasma
356 clearance half-life (~ 20 min) (6) as compared to monoclonal antibodies (~114 hours)—yields
357 optimal AIT of only a few hours (21,27) as demonstrated here. However, the ability of PAI to
358 provide stable contrast and high tumor differentiation starting at 30 min (and extending for hours)
359 highlights the potential for in-surgical suite administration of PAI, reducing complexities in patient
360 appointments and surgical timing that can occur with SAI.

361

362 **Conclusions**

363 PAI has the potential to broadly impact the clinical implementation of fluorescence guided surgery.
364 PAI diagnosed tongue SCCs with high accuracy, which was less sensitive to inter-patient variabil-
365 ity. PAI accurately represented the true molecular heterogeneity of receptor expression in tumors
366 and could be used to image over a wide range of clinically applicable resolutions. In addition, PAI
367 demonstrated the potential to facilitate flexibility within the surgical setting by decreasing the time
368 from imaging agent administration to the start of resection while maintaining high diagnostic ac-
369 curacy. We propose the use of PAI as an innovative molecular imaging method that will improve
370 the diagnostic accuracy and efficiency of FGS.

371

372 **List of abbreviations**

373 FGS: Fluorescence guided surgery; PAI: Paired-agent imaging; EGFR: Epidermal growth factor
374 receptor; SAI: Single-agent imaging; BP: Binding potential; GLP: Good Laboratory Practice;
375 PBS: phosphate buffered saline; STP: Single-time point; NF: Normalization factor; ROI: Re-
376 gions-of-interest; AUC: Under the curve; ROC: Receiver operating characteristic; CVR: Con-
377 trast-to-Variance Ratio; PPV: Positive prediction value; NPV: Negative prediction value; TBR:
378 Tumor-to-background ratio; AIT: Administration-to-imaging time

379

380

381 **Declarations**

382 **Ethics approval and consent to participate**

383 All animal procedures were approved by the Dartmouth Institutional Animal Care and Use Com-
384 mittee (IACUC) and conducted according to NIH-OLAW and AAAALAC guidelines.

385 **Consent for publication**

386 Not applicable.

387 **Availability of data and materials**

388 All data generated or analyzed during this study are included in this published article.

389 **Competing interests**

390 KSS reports an ongoing academic-industrial relationship for the development and clinical testing
391 of ABY-029 with LI-COR Biosciences and Affibody AB, and personal fees from LI-COR and
392 American Institute for Biological Sciences.

393 **Funding**

394 This work was funded by the grant R37 CA212187 (KSS). The production of ABY-029 was pre-
395 viously funded by R01 CA167413, flow cytometry was performed with support from 5P30
396 CA023108-41.

397 **Authors' contribution**

398 CW designed the research, performed experiments, analyzed data and wrote the manuscript. MF,
399 JRG, SH, and PJH helped perform experiments, analyzed data, and/or interpreted data. EYC, KMT
400 helped design the study and interpreted data. KSS designed the research, provided the funding,
401 interpreted data, and supervised the experiments. All authors read, edited, and approved the final
402 manuscript.

403 **Acknowledgements**

404 The authors would like to acknowledge the gift of ABY-029 (R01 CA167413, PI Keith Paulsen),
405 EGFR quantification experiments were carried out in DartLab, the Immune Monitoring and Flow
406 Cytometry Shared Resource at the Norris Cotton Cancer Center at Dartmouth, with NCI Cancer
407 Center Support Grant with support from 5P30 CA023108-41.

408 **REFERENCES**

- 409 1. Binahmed A, Nason RW, Abdoh AA. The clinical significance of the positive surgical mar-
410 gin in oral cancer. *Oral oncology*. 2007;43(8):780–784.
- 411 2. Grandis JR, Melhem MF, Gooding WE, Day R, Holst VA, Wagener MM, et al. Levels of
412 TGF- α and EGFR protein in head and neck squamous cell carcinoma and patient survival.
413 *JNCI: Journal of the National Cancer Institute*. 1998;90(11):824–832.
- 414 3. Santini J, Formento J-L, Francoual M, Milano G, Schneider M, Dassonville O, et al. Charac-
415 terization, quantification, and potential clinical value of the epidermal growth factor recep-
416 tor in head and neck squamous cell carcinomas. *Head & neck*. 1991;13(2):132–139.
- 417 4. Gao RW, Teraphongphom N, de Boer E, van den Berg NS, Divi V, Kaplan MJ, et al. Safety
418 of panitumumab-IRDye800CW and cetuximab-IRDye800CW for fluorescence-guided sur-
419 gical navigation in head and neck cancers. 2018;8(9):2488.
- 420 5. Rosenthal EL, Warram JM, De Boer E, Chung TK, Korb ML, Brandwein-Gensler M, et al.
421 Safety and tumor specificity of cetuximab-IRDye800 for surgical navigation in head and
422 neck cancer. *Clinical Cancer Research*. 2015;21(16):3658–3666.

- 423 6. Samkoe KS, Gunn JR, Marra K, Hull SM, Moodie KL, Feldwisch J, et al. Toxicity and phar-
424 macokinetic profile for single-dose injection of ABY-029: a fluorescent anti-EGFR syn-
425 thetic affibody molecule for human use. *Molecular Imaging and Biology*. 2017;19(4):512–
426 521.
- 427 7. Voskuil FJ, de Jongh SJ, Hooghiemstra WTR, Linssen MD, Steinkamp PJ, de Visscher
428 SAHJ, et al. Fluorescence-guided imaging for resection margin evaluation in head and neck
429 cancer patients using cetuximab-800CW: A quantitative dose-escalation study.
430 *Theranostics*. 2020 Mar 4;10(9):3994–4005.
- 431 8. Linssen MD, ter Weele EJ, Allersma DP, Lub-de Hooge MN, van Dam GM, Jorritsma-Smit
432 A, et al. Roadmap for the Development and Clinical Translation of Optical Tracers Cetuxi-
433 mab-800CW and Trastuzumab-800CW. 2019;60(3):418–23.
- 434 9. Gao RW, Teraphongphom NT, van den Berg NS, Martin BA, Oberhelman NJ, Divi V, et al.
435 Determination of tumor margins with surgical specimen mapping using near-infrared fluo-
436 rescence. *Cancer research*. 2018;78(17):5144–5154.
- 437 10. Rosenthal EL, Moore LS, Tipirneni K, de Boer E, Stevens TM, Hartman YE, et al. Sensitiv-
438 ity and specificity of cetuximab-IRDye800CW to identify regional metastatic disease in
439 head and neck cancer. *Clinical Cancer Research*. 2017;23(16):4744–4752.
- 440 11. van Keulen S, Nishio N, Birkeland A, Fakurnejad S, Martin B, Forouzanfar T, et al. The
441 Sentinel Margin: Intraoperative *Ex Vivo* Specimen Mapping Using Relative
442 Fluorescence Intensity. 2019;25(15):4656–62.

- 443 12. Tichauer KM, Samkoe KS, Klubben WS, Hasan T, Pogue BW. Advantages of a dual-tracer
444 model over reference tissue models for binding potential measurement in tumors. *Physics in*
445 *Medicine & Biology*. 2012;57(20):6647.
- 446 13. Samkoe KS, Tichauer KM, Gunn JR, Wells WA, Hasan T, Pogue BW. Quantitative in vivo
447 immunohistochemistry of epidermal growth factor receptor using a receptor concentration
448 imaging approach. *Cancer research*. 2014;74(24):7465–7474.
- 449 14. Tichauer KM, Samkoe KS, Gunn JR, Kanick SC, Hoopes PJ, Barth RJ, et al. Microscopic
450 lymph node tumor burden quantified by macroscopic dual-tracer molecular imaging. *Nature*
451 *medicine*. 2014;20(11):1348.
- 452 15. Reagan-Shaw S, Nihal M, Ahmad N. Dose translation from animal to human studies revis-
453 ited. *FASEB J*. 2008 Mar;22(3):659–61.
- 454 16. Tichauer KM, Samkoe KS, Sexton KJ, Gunn JR, Hasan T, Pogue BW. Improved tumor con-
455 trast achieved by single time point dual-reporter fluorescence imaging. *J Biomed Opt*. 2012
456 Jun;17(6):066001.
- 457 17. Ruifrok AC, Johnston DA. Quantification of histochemical staining by color deconvolution.
458 *Analytical and quantitative cytology and histology*. 2001;23(4):291–299.
- 459 18. Elliott JT, Marra K, Evans LT, Davis SC, Samkoe KS, Feldwisch J, et al. Simultaneous In
460 Vivo Fluorescent Markers for Perfusion, Protoporphyrin Metabolism, and EGFR Expres-
461 sion for Optically Guided Identification of Orthotopic Glioma. *Clin Cancer Res*. 2017 May
462 1;23(9):2203–12.

- 463 19. DSouza AV, Lin H, Henderson ER, Samkoe KS, Pogue BW. Review of fluorescence guided
464 surgery systems: identification of key performance capabilities beyond indocyanine green
465 imaging. *J Biomed Opt.* 2016 01;21(8):80901.
- 466 20. Tichauer K, Samkoe K, Sexton K, Hextrum S, Yang H, Klubben WS, et al. In Vivo Quantifi-
467 cation of Tumor Receptor Binding Potential with Dual-Reporter Molecular Imaging. *Mo-*
468 *lecular Imaging and Biology.* 2012 Oct 1;14(5):584–92.
- 469 21. Samkoe KS, Sardar HS, Bates BD, Tselepidakis NN, Gunn JR, Hoffer-Hawlik KA, et al.
470 Preclinical imaging of epidermal growth factor receptor with ABY-029 in soft-tissue sar-
471 coma for fluorescence-guided surgery and tumor detection. *J Surg Oncol.* 2019
472 Jun;119(8):1077–86.
- 473 22. Dual-agent fluorescent labeling of soft-tissue sarcomas improves the contrast based upon tar-
474 geting both interstitial and cellular components of the tumor milieu - Sardar - - *Journal of*
475 *Surgical Oncology - Wiley Online Library [Internet].* [cited 2020 Sep 16]. Available from:
476 <https://onlinelibrary.wiley.com/doi/full/10.1002/jso.26190>
- 477 23. Hu Z, Fang C, Li B, Zhang Z, Cao C, Cai M, et al. First-in-human liver-tumour surgery
478 guided by multispectral fluorescence imaging in the visible and near-infrared-I/II windows.
479 *Nature Biomedical Engineering.* 2020 Mar;4(3):259–71.
- 480 24. Moore LS, Rosenthal EL, de Boer E, Prince AC, Patel N, Richman JM, et al. Effects of an
481 Unlabeled Loading Dose on Tumor-Specific Uptake of a Fluorescently Labeled Antibody
482 for Optical Surgical Navigation. *Molecular Imaging and Biology.* 2016;19(4):610–6.

- 483 25. Nishio N, van den Berg NS, van Keulen S, Martin BA, Fakurnejad S, Zhou Q, et al. Optimal
484 Dosing Strategy for Fluorescence-Guided Surgery with Panitumumab-IRDye800CW in
485 Head and Neck Cancer. *Molecular Imaging and Biology*. 2020 Feb 1;22(1):156–64.
- 486 26. Judy RP, Keating JJ, DeJesus EM, Jiang JX, Okusanya OT, Nie S, et al. Quantification of
487 tumor fluorescence during intraoperative optical cancer imaging. *Scientific Reports*. 2015
488 Nov 13;5(1):16208.
- 489 27. de Souza AL, Marra K, Gunn J, Samkoe KS, Hoopes PJ, Feldwisch J, et al. Fluorescent Af-
490 fibody Molecule Administered In Vivo at a Microdose Level Labels EGFR Expressing Gli-
491 oma Tumor Regions. *Molecular Imaging and Biology*. 2017 Feb;19(1):41–8.

492

493

494

495

496

497

498

499

500

501

502

503

504

505 **Figure Captions**

506 **Figure 1.** Schematic of experimental procedures. (A) Mice, with xenograft murine tongue tumors,
507 were administrated ABY-029 and IRDye 700DX by tail vein injection. *Inset* - a pictorial represen-
508 tation of the paired-agent distribution 3-hours after administration, where both agents are present
509 due to non-specific binding and uptake in all tissues, while only ABY-029 specifically bound to
510 receptors. After sacrifice, the tongue is removed and bisected. Tumor and normal tissue fluores-
511 cence was imaged using Odyssey CLx. (B) Binding potential (BP) maps representing available
512 EGFR concentrations were created by ratioing targeted and normalized untargeted fluorescence.
513 For further impartial analysis, pathological and fluorescence images were digitally aligned and co-
514 registered.

515
516 **Figure 2.** PAI exhibits ability to distinguish normal and tumor tissues using average ROI signal
517 intensity. (A) After image co-registration, pathologist-defined ROIs of tumor, normal tongue (NT),
518 and salivary glands (SG) on H&E sections were translated manually to the digitally aligned images
519 of EGFR IHC, ABY-029, and BP. (B) The distribution of signal in tumor and normal tissue (leg
520 muscle (LM), NT, and SG) were compared for the ABY-029 fluorescence and BP. Tumor ROIs
521 were analyzed using: pathologist-determined tumor (entire tumor) and the EGFR-positive pixels
522 within the pathologist-determined tumor. (C). The average signal from each ROI was plotted for
523 all animals. For clarity, only the groups where the means were *not* statistically different ($p > 0.05$)
524 are shown.

525
526 **Figure 3.** Pixel-by-pixel analysis demonstrates PAI has higher diagnostic accuracy than SAI. (A)
527 ROC curve analysis was performed for each IRDye 700DX, ABY-029, and BP using EGFR IHC

528 as the gold standard. In all individual mice, BP images have higher AUC than ABY-029 and IRDye
529 700DX images. (B) Cohort data from each individual tumor group ($n = 6$ or 7) and All Cell Lines
530 ($n = 20$), also demonstrate that BP maps have higher AUC compared to ABY-029 alone. Cohort
531 statistics generated using the optimum ROC cut off point, and the highest statistic parameter is
532 highlighted in green. BP performance is superior to ABY-029 with the exception of sensitivity and
533 negative predictive value (NPV) in the Det 562 cell line. PPV = positive predictive value, Diag.
534 Acc. = diagnostic accuracy.

535

536 **Figure 4.** EGFR heterogeneity is most accurately represented by PAI determined BP. BP and
537 ABY-029 fluorescence images were compared to EGFR IHC on a pixel-to-pixel basis using the
538 Pearson correlation coefficient (r). (A) The image pyramid method was used to correct any poten-
539 tial misalignment between pathological and fluorescence images by reducing pixel resolution,
540 which resulted in increased correlation to IHC for all image types. In all four levels of the image
541 pyramid, correlation to EGFR IHC was stronger for BP than ABY-029 or IRDye 700DX. (B) The
542 average and relative change in r were plotted against spatial resolution. Pearson correlation coef-
543 ficients were determined for Level 2 images ($168 \mu\text{m}$) of all three tumor lines. A representative
544 scatter plot for each tumor line is shown, in addition to the cohort data at the far right. BP shows a
545 strong positive linear correlation to EGFR IHC in all three tumor groups and is higher than that of
546 ABY-029.

547

548 **Figure 5.** Comparison of administration-to-imaging time for PAI and SAI. (A) A representative
549 image of the xenograft tongue tumors are shown for each SAI agent and PAI BP at each time point.
550 The tumor cohort average for each time point is plotted to the right. BP is fairly constant over the

551 5-hour period, while fluorescence signal decreases for IRDye 700DX and increases for ABY-029
552 over time. (B) BP map determined CVR is significantly higher ($p < 0.05$) than that of ABY-029
553 over the first 2 hours after administration, suggesting that BP provides a more stable tumor contrast
554 measure. (C). ROC analysis indicates diagnostic abilities of both imaging methods improve over
555 time; however, BP outperforms ABY-029 images, especially at short administration-to-imaging
556 time points.

557

558 **Supplementary information**

559
560 Supplementary Figure 1: Determining doses of paired-agent imaging using auto-fluorescence. **A**,

561 For each tumor type a representative example of the autofluorescence in a tongue tumor from FaDu,
562 Detroit 562 and A431 cell lines are shown for the 700 and 800 nm channels of the Odyssey CLx
563 scanner and compared to standard H&E and epidermal growth factor receptor (EGFR) immuno-
564 histochemistry (IHC). **B**, The binding potential (BP) calculated for each naïve tongue is shown in
565 the corresponding box plot.

566 Supplementary Figure 2: **A**, Fluorescence measurements in tumor and normal tissue are shown in
567 the 700 and 800 channels for auto-fluorescence, 1X dose of ABY-029 and IRDye 700DX (mouse
568 equivalent to the human microdose, 30 nanomoles), and a 1X dose of ABY-029 and 10X dose of
569 IRDye 700DX. **B**, The naïve and 10X dose values of IRDye 700DX are shown for each tumor
570 type.

571 Supplementary Figure 3: The effect of the normalization factor (NF) on image contrast. As the
572 normalization ratio increases, the overall signal decreases. This results in a constant contrast-to-
573 variance ratio (CVR) that is stable when NF is varied. However, tumor-to-background ratio (TBR)
574 increases as the signal in the normal tissue (the denominator) decreases. These results indicate that
575 TBR is an unstable measure for binding potential and con not be used to compare to single agent
576 fluorescence.

577 Supplementary Figure 4: Image overlays created using *imshowpair* in Matlab allow visual assess-
578 ment of spatial alignment between IHC and BP images. In the Checkerboard overlay, IHC is in
579 RGB (brown pixels) while the BP map is a grey scale image.

580 Supplementary Figure 5: EGFR molecules per cell line for squamous cell carcinomas determined
581 by quantitative flow cytometry. Cell lines used for this study are indicated in green.

582 Supplementary Table 1: Summary of individual trial and average values of EGFR per cell deter-
583 mined by quantitative flow cytometry

584

585

586

Figures

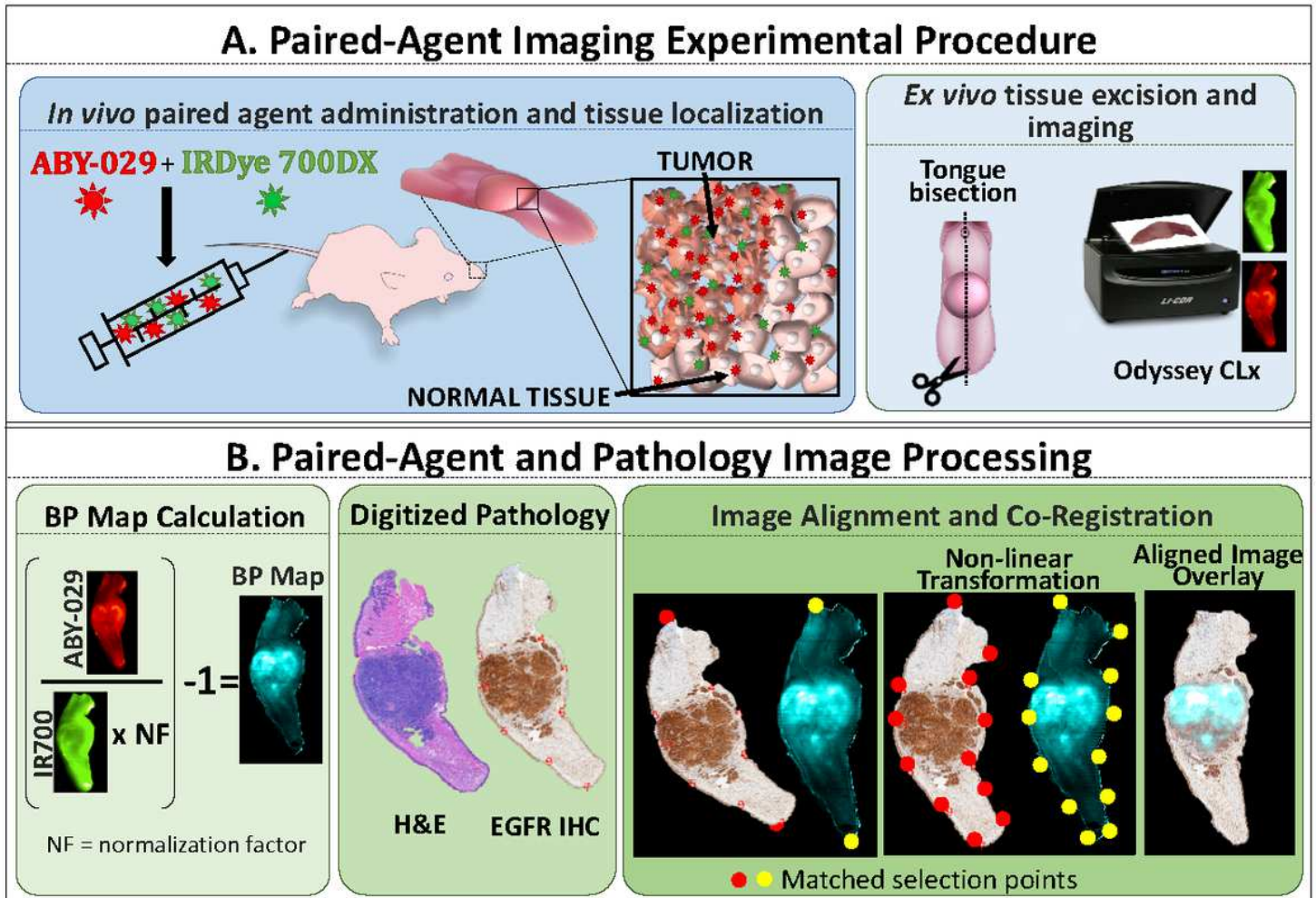


Figure 1

Schematic of experimental procedures. (A) Mice, with xenograft murine tongue tumors, were administered ABY-029 and IRDye 700DX by tail vein injection. Inset - a pictorial representation of the paired-agent distribution 3-hours after administration, where both agents are present due to non-specific binding and uptake in all tissues, while only ABY-029 specifically bound to receptors. After sacrifice, the tongue is removed and bisected. Tumor and normal tissue fluorescence was imaged using Odyssey CLx. (B) Binding potential (BP) maps representing available EGFR concentrations were created by ratioing targeted and normalized untargeted fluorescence. For further impartial analysis, pathological and fluorescence images were digitally aligned and co-registered.

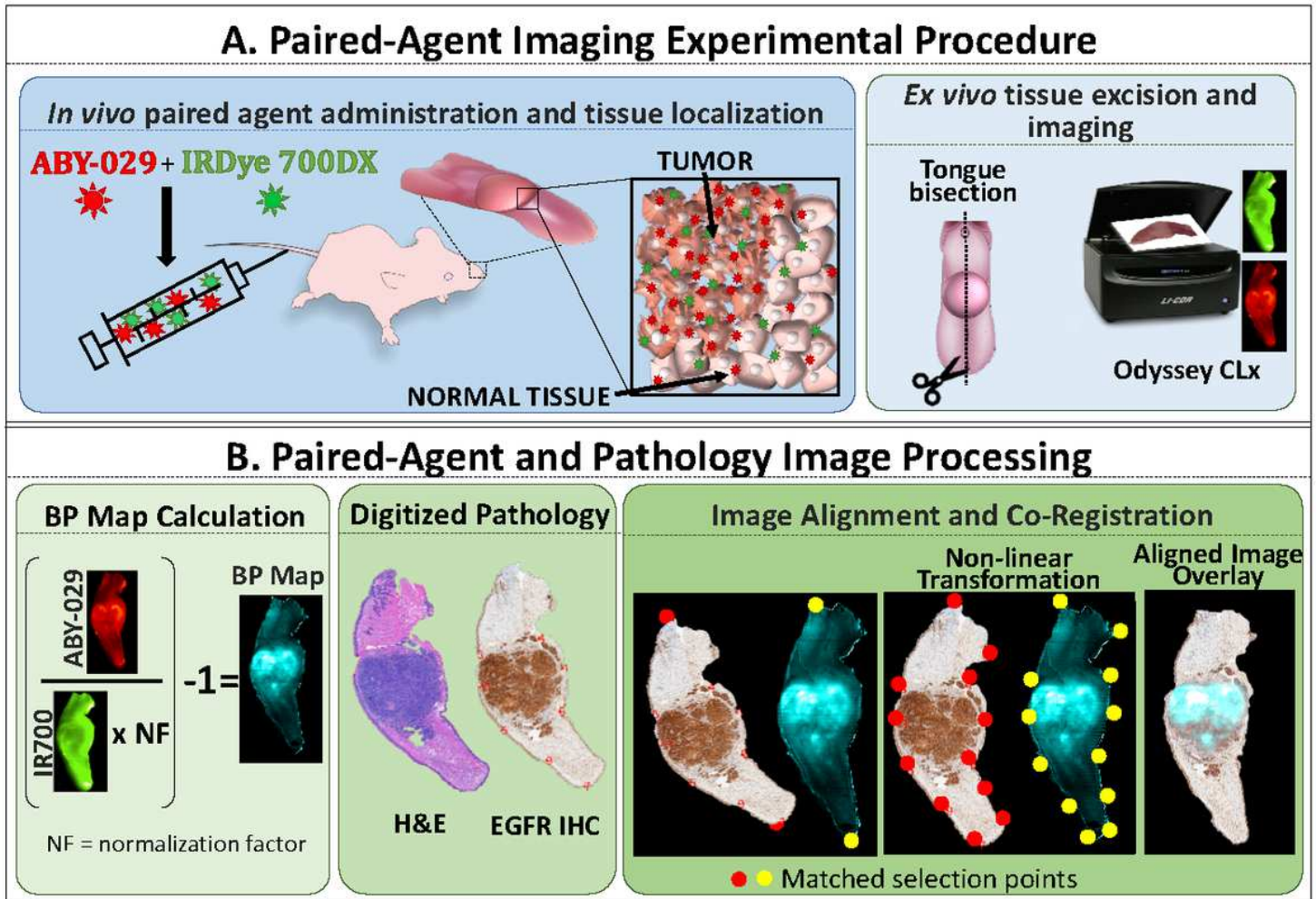


Figure 1

Schematic of experimental procedures. (A) Mice, with xenograft murine tongue tumors, were administrated ABY-029 and IRDye 700DX by tail vein injection. Inset - a pictorial representation of the paired-agent distribution 3-hours after administration, where both agents are present due to non-specific binding and uptake in all tissues, while only ABY-029 specifically bound to receptors. After sacrifice, the tongue is removed and bisected. Tumor and normal tissue fluorescence was imaged using Odyssey CLx. (B) Binding potential (BP) maps representing available EGFR concentrations were created by ratioing targeted and normalized untargeted fluorescence. For further impartial analysis, pathological and fluorescence images were digitally aligned and co-registered.

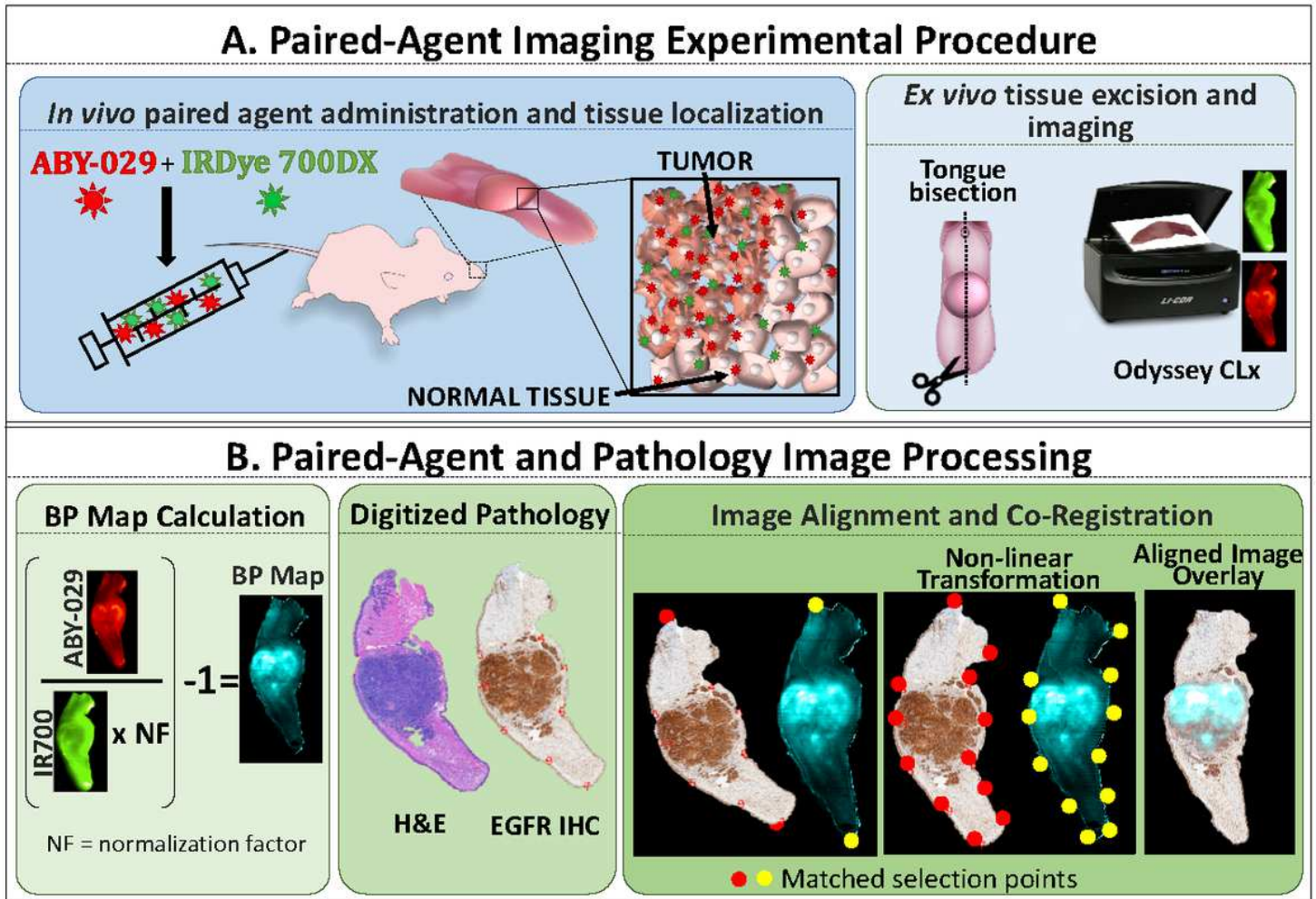


Figure 1

Schematic of experimental procedures. (A) Mice, with xenograft murine tongue tumors, were administrated ABY-029 and IRDye 700DX by tail vein injection. Inset - a pictorial representation of the paired-agent distribution 3-hours after administration, where both agents are present due to non-specific binding and uptake in all tissues, while only ABY-029 specifically bound to receptors. After sacrifice, the tongue is removed and bisected. Tumor and normal tissue fluorescence was imaged using Odyssey CLx. (B) Binding potential (BP) maps representing available EGFR concentrations were created by ratioing targeted and normalized untargeted fluorescence. For further impartial analysis, pathological and fluorescence images were digitally aligned and co-registered.

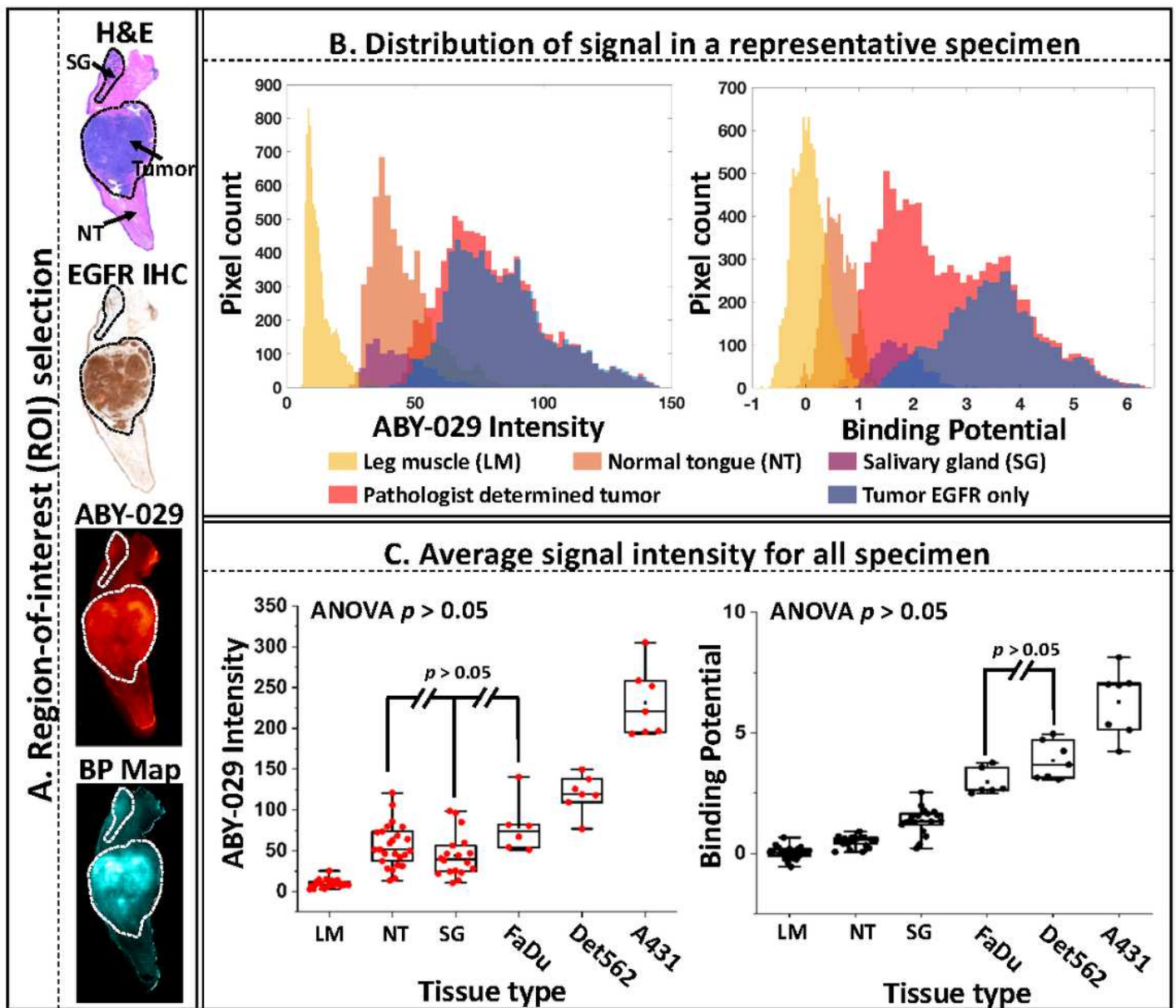


Figure 2

PAI exhibits ability to distinguish normal and tumor tissues using average ROI signal intensity. (A) After image co-registration, pathologist-defined ROIs of tumor, normal tongue (NT), and salivary glands (SG) on H&E sections were translated manually to the digitally aligned images of EGFR IHC, ABY-029, and BP. (B) The distribution of signal in tumor and normal tissue (leg muscle (LM), NT, and SG) were compared for the ABY-029 fluorescence and BP. Tumor ROIs were analyzed using: pathologist-determined tumor (entire tumor) and the EGFR-positive pixels within the pathologist-determined tumor. (C). The average signal from each ROI was plotted for all animals. For clarity, only the groups where the means were not statistically different ($p > 0.05$) are shown.

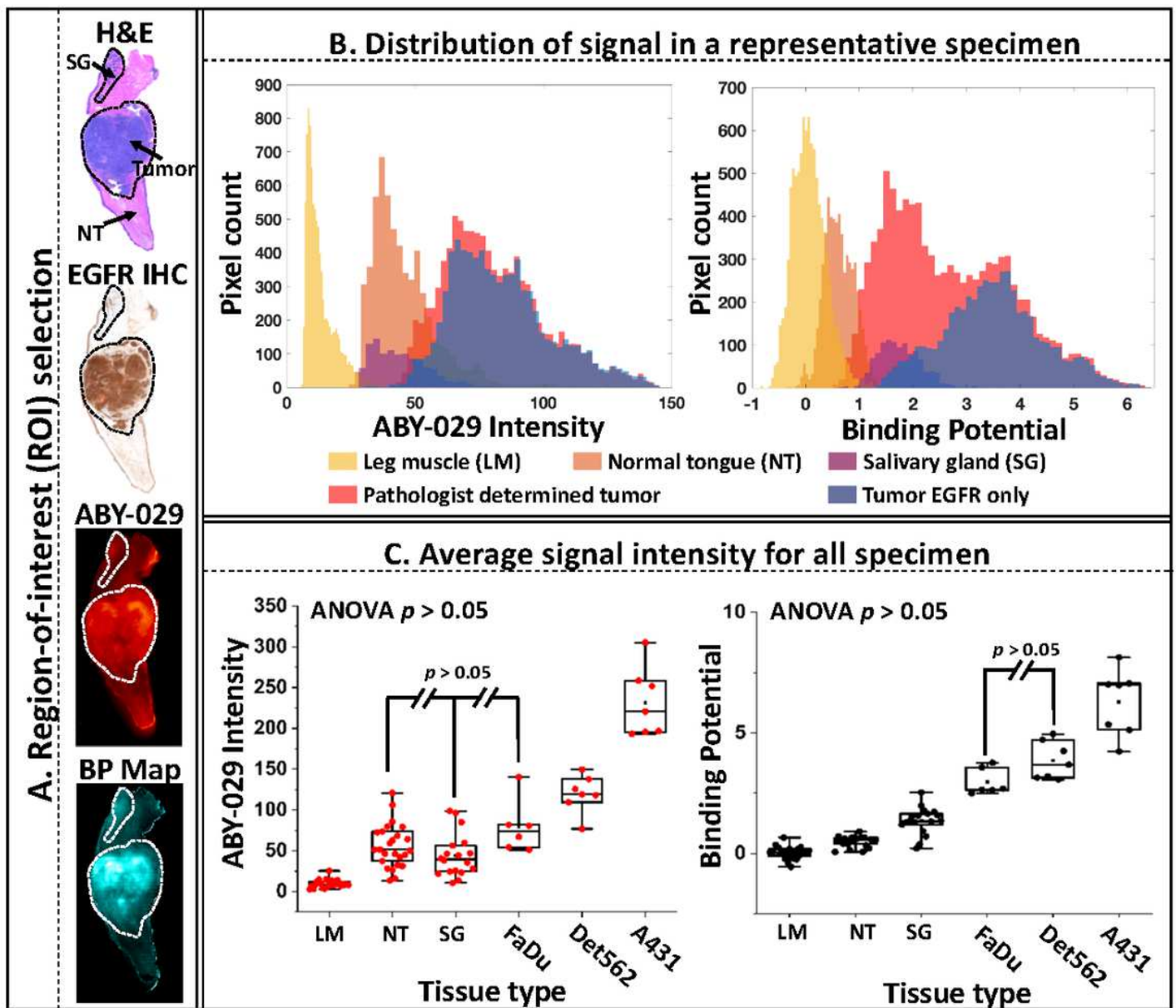


Figure 2

PAI exhibits ability to distinguish normal and tumor tissues using average ROI signal intensity. (A) After image co-registration, pathologist-defined ROIs of tumor, normal tongue (NT), and salivary glands (SG) on H&E sections were translated manually to the digitally aligned images of EGFR IHC, ABY-029, and BP. (B) The distribution of signal in tumor and normal tissue (leg muscle (LM), NT, and SG) were compared for the ABY-029 fluorescence and BP. Tumor ROIs were analyzed using: pathologist-determined tumor (entire tumor) and the EGFR-positive pixels within the pathologist-determined tumor. (C). The average signal from each ROI was plotted for all animals. For clarity, only the groups where the means were not statistically different ($p > 0.05$) are shown.

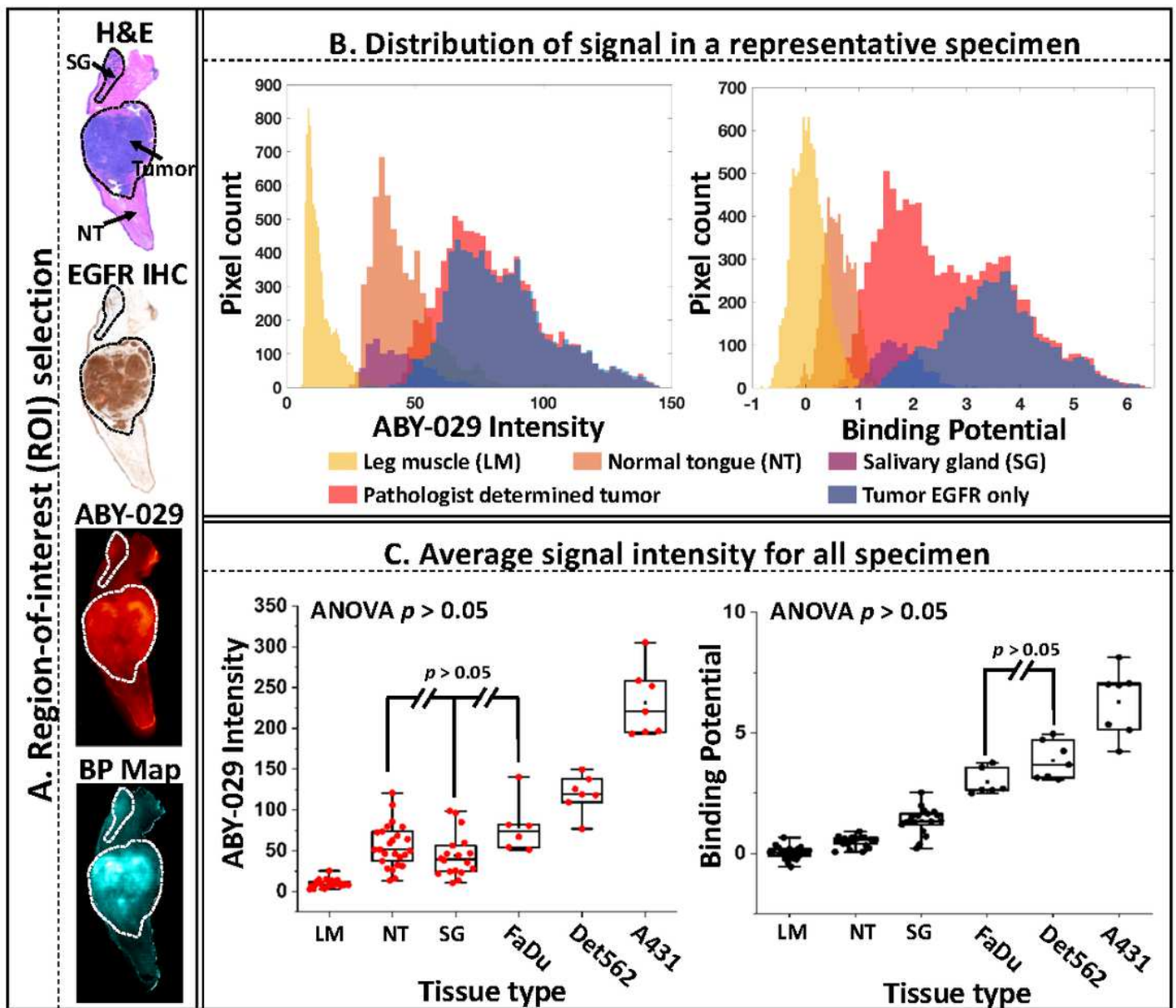


Figure 2

PAI exhibits ability to distinguish normal and tumor tissues using average ROI signal intensity. (A) After image co-registration, pathologist-defined ROIs of tumor, normal tongue (NT), and salivary glands (SG) on H&E sections were translated manually to the digitally aligned images of EGFR IHC, ABY-029, and BP. (B) The distribution of signal in tumor and normal tissue (leg muscle (LM), NT, and SG) were compared for the ABY-029 fluorescence and BP. Tumor ROIs were analyzed using: pathologist-determined tumor (entire tumor) and the EGFR-positive pixels within the pathologist-determined tumor. (C). The average signal from each ROI was plotted for all animals. For clarity, only the groups where the means were not statistically different ($p > 0.05$) are shown.

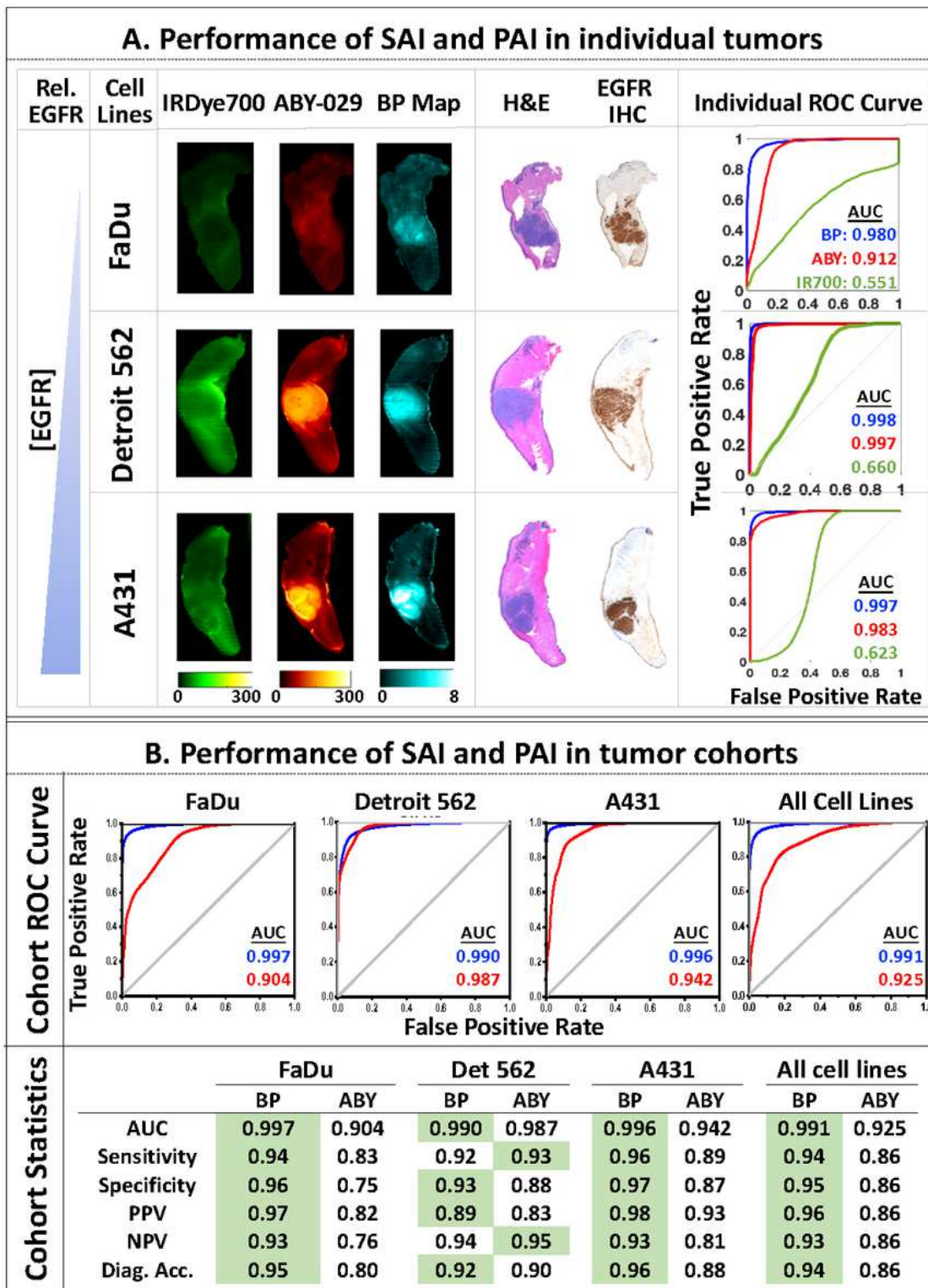


Figure 3

Pixel-by-pixel analysis demonstrates PAI has higher diagnostic accuracy than SAI. (A) ROC curve analysis was performed for each IRDye 700DX, ABY-029, and BP using EGFR IHC as the gold standard. In all individual mice, BP images have higher AUC than ABY-029 and IRDye 700DX images. (B) Cohort data from each individual tumor group (n = 6 or 7) and All Cell Lines (n = 20), also demonstrate that BP maps have higher AUC compared to ABY-029 alone. Cohort statistics generated using the optimum ROC cut off

point, and the highest statistic parameter is highlighted in green. BP performance is superior to ABY-029 with the exception of sensitivity and negative predictive value (NPV) in the Det 562 cell line. PPV = positive predictive value, Diag. Acc. = diagnostic accuracy.

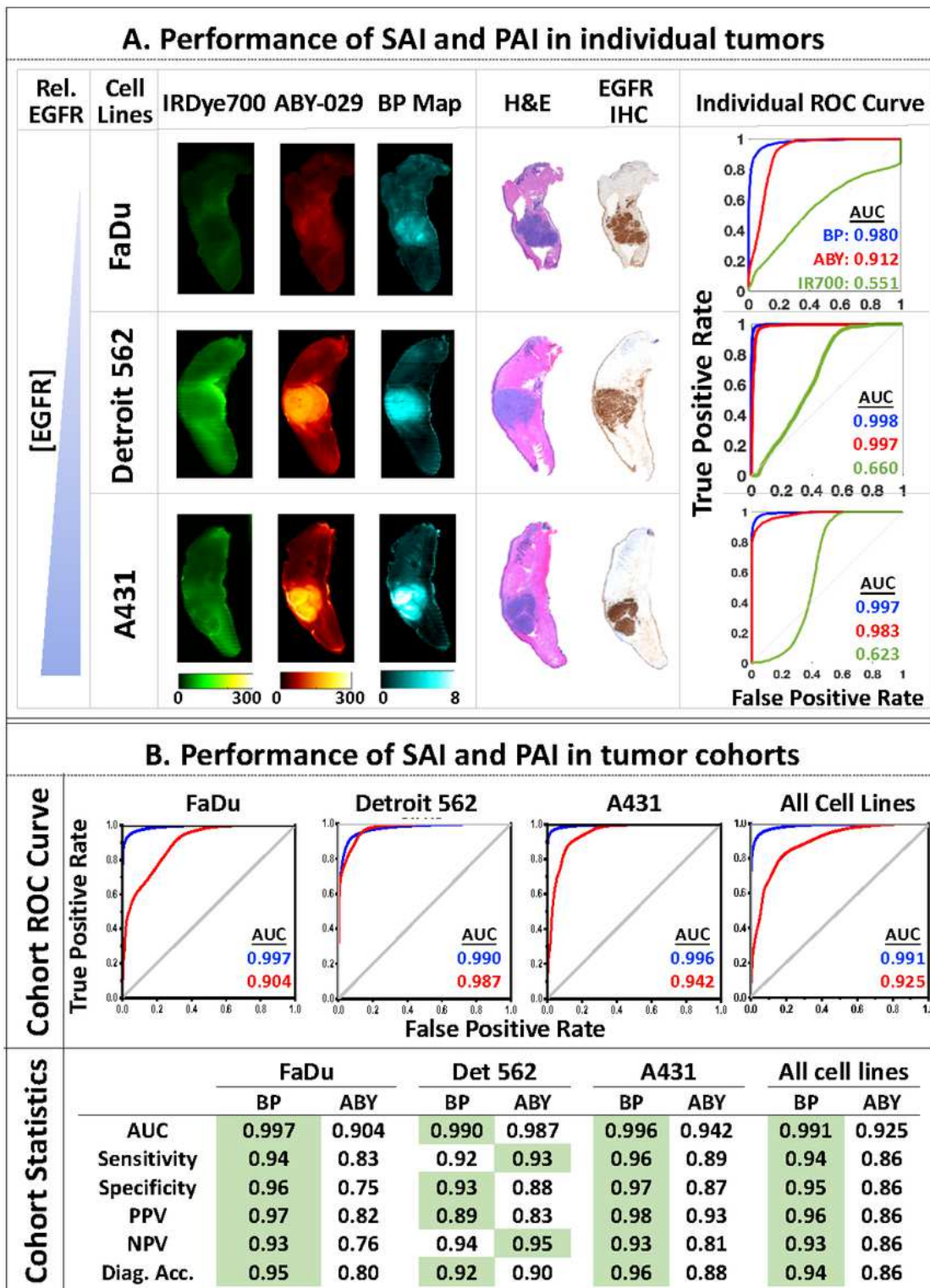


Figure 3

Pixel-by-pixel analysis demonstrates PAI has higher diagnostic accuracy than SAI. (A) ROC curve analysis was performed for each IRDye 700DX, ABY-029, and BP using EGFR IHC as the gold standard. In all

individual mice, BP images have higher AUC than ABY-029 and IRDye 700DX images. (B) Cohort data from each individual tumor group (n = 6 or 7) and All Cell Lines (n = 20), also demonstrate that BP maps have higher AUC compared to ABY-029 alone. Cohort statistics generated using the optimum ROC cut off point, and the highest statistic parameter is highlighted in green. BP performance is superior to ABY-029 with the exception of sensitivity and negative predictive value (NPV) in the Det 562 cell line. PPV = positive predictive value, Diag. Acc. = diagnostic accuracy.

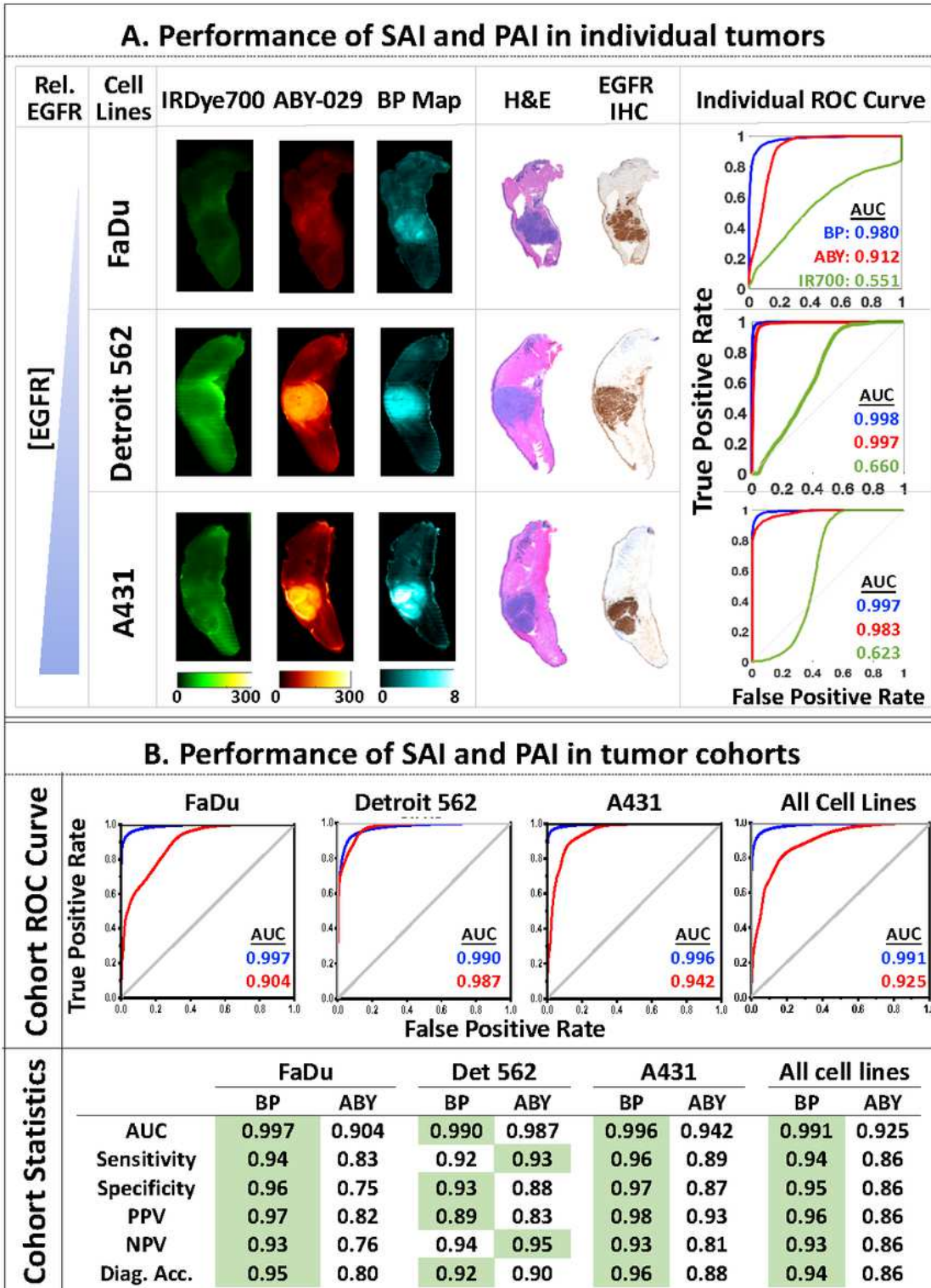


Figure 3

Pixel-by-pixel analysis demonstrates PAI has higher diagnostic accuracy than SAI. (A) ROC curve analysis was performed for each IRDye 700DX, ABY-029, and BP using EGFR IHC as the gold standard. In all individual mice, BP images have higher AUC than ABY-029 and IRDye 700DX images. (B) Cohort data from each individual tumor group ($n = 6$ or 7) and All Cell Lines ($n = 20$), also demonstrate that BP maps have higher AUC compared to ABY-029 alone. Cohort statistics generated using the optimum ROC cut off point, and the highest statistic parameter is highlighted in green. BP performance is superior to ABY-029 with the exception of sensitivity and negative predictive value (NPV) in the Det 562 cell line. PPV = positive predictive value, Diag. Acc. = diagnostic accuracy.

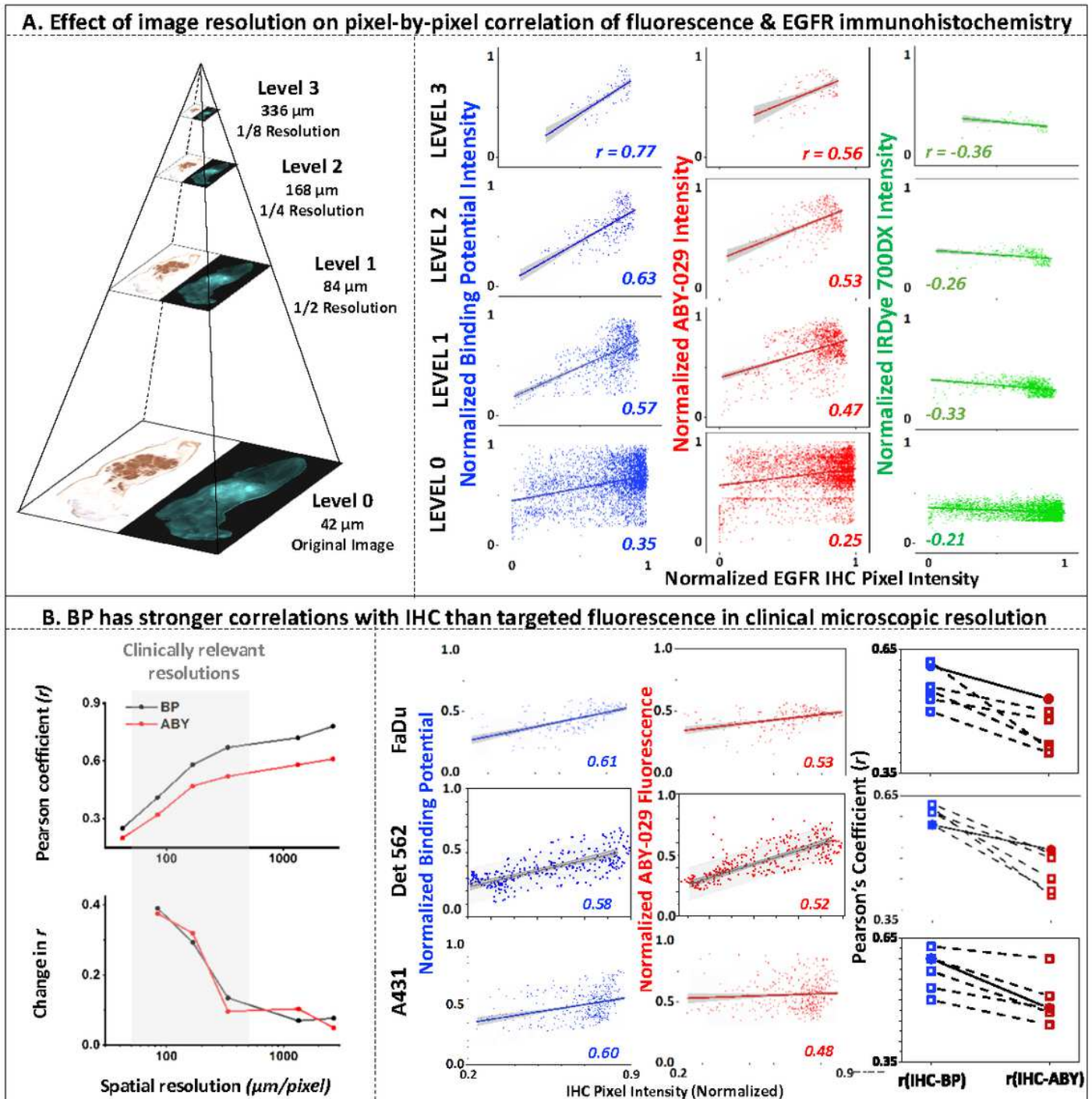


Figure 4

EGFR heterogeneity is most accurately represented by PAI determined BP. BP and ABY-029 fluorescence images were compared to EGFR IHC on a pixel-to-pixel basis using the Pearson correlation coefficient (r). (A) The image pyramid method was used to correct any potential misalignment between pathological and fluorescence images by reducing pixel resolution, which resulted in increased correlation to IHC for all image types. In all four levels of the image pyramid, correlation to EGFR IHC was stronger for BP than ABY-029 or IRDye 700DX. (B) The average and relative change in r were plotted against spatial resolution. Pearson correlation coefficients were determined for Level 2 images (168 μm) of all three tumor lines. A representative scatter plot for each tumor line is shown, in addition to the cohort data at the far right. BP shows a strong positive linear correlation to EGFR IHC in all three tumor groups and is higher than that of ABY-029.

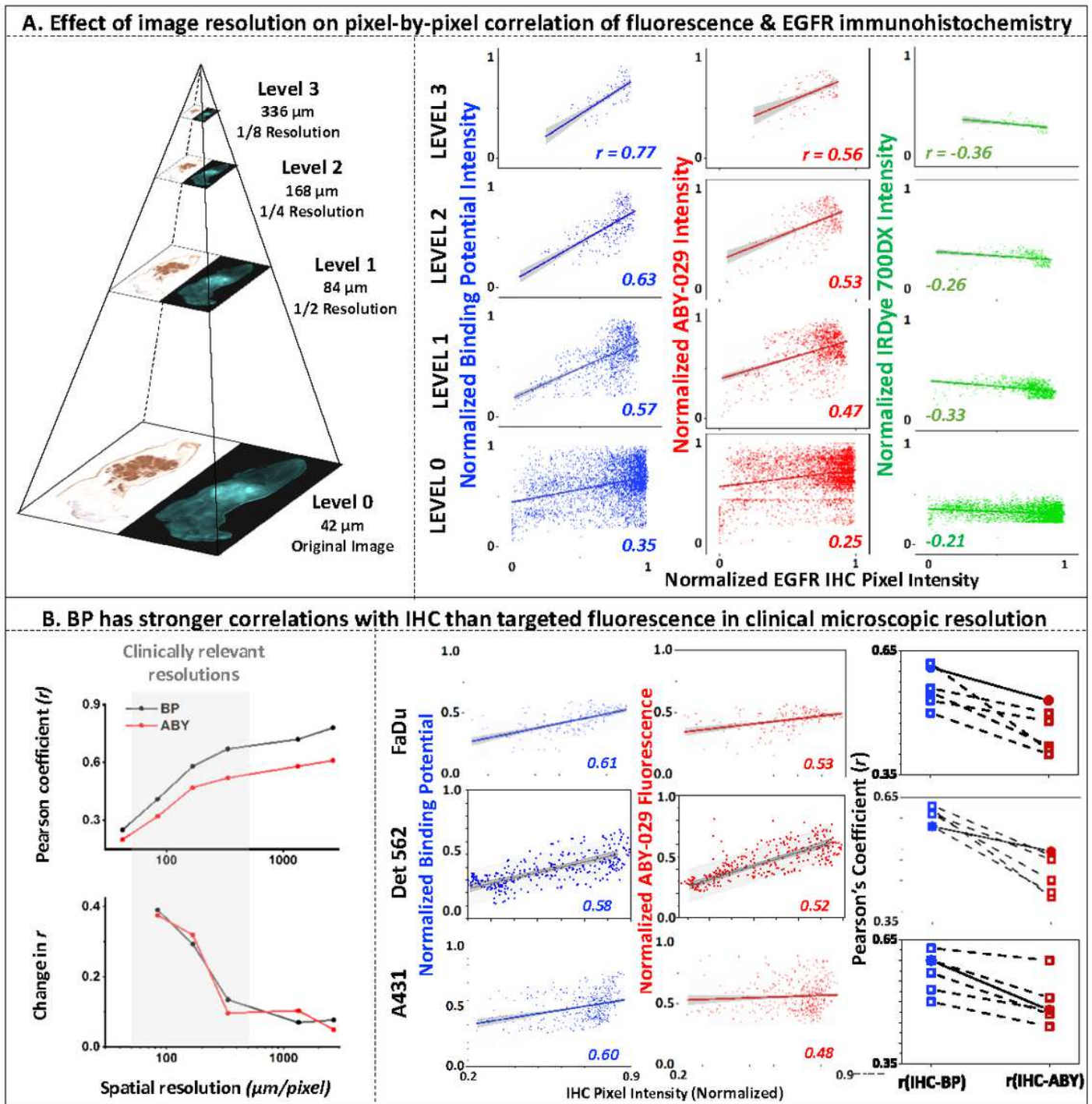


Figure 4

EGFR heterogeneity is most accurately represented by PAI determined BP. BP and ABY-029 fluorescence images were compared to EGFR IHC on a pixel-to-pixel basis using the Pearson correlation coefficient (r). (A) The image pyramid method was used to correct any potential misalignment between pathological and fluorescence images by reducing pixel resolution, which resulted in increased correlation to IHC for all image types. In all four levels of the image pyramid, correlation to EGFR IHC was stronger for BP than ABY-029 or IRDye 700DX. (B) The average and relative change in r were plotted against spatial resolution.

Pearson correlation coefficients were determined for Level 2 images (168 μm) of all three tumor lines. A representative scatter plot for each tumor line is shown, in addition to the cohort data at the far right. BP shows a strong positive linear correlation to EGFR IHC in all three tumor groups and is higher than that of ABY-029.

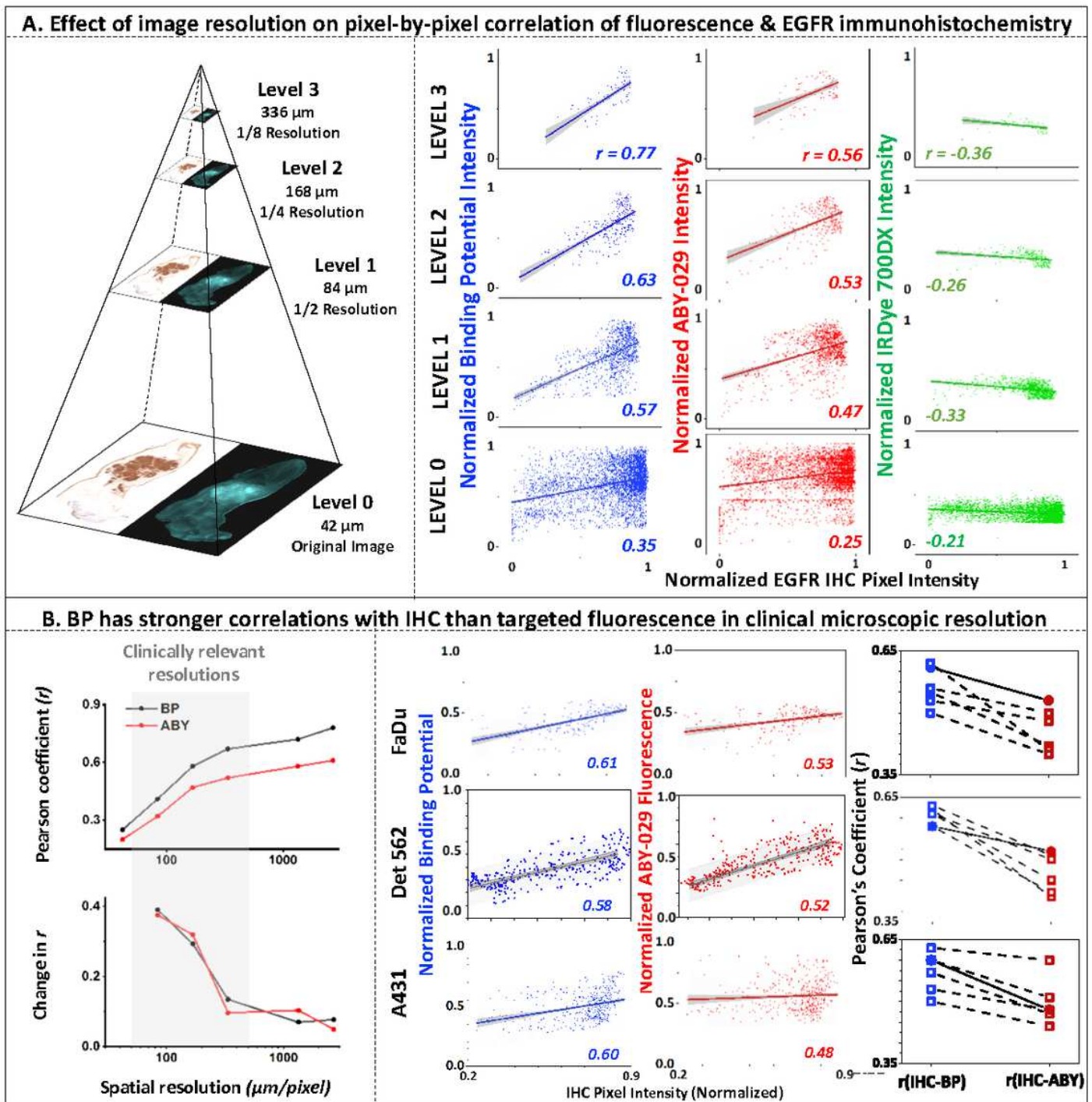


Figure 4

EGFR heterogeneity is most accurately represented by PAI determined BP. BP and ABY-029 fluorescence images were compared to EGFR IHC on a pixel-to-pixel basis using the Pearson correlation coefficient (r).

(A) The image pyramid method was used to correct any potential misalignment between pathological and fluorescence images by reducing pixel resolution, which resulted in increased correlation to IHC for all image types. In all four levels of the image pyramid, correlation to EGFR IHC was stronger for BP than ABY-029 or IRDye 700DX. (B) The average and relative change in r were plotted against spatial resolution. Pearson correlation coefficients were determined for Level 2 images (168 μm) of all three tumor lines. A representative scatter plot for each tumor line is shown, in addition to the cohort data at the far right. BP shows a strong positive linear correlation to EGFR IHC in all three tumor groups and is higher than that of ABY-029.

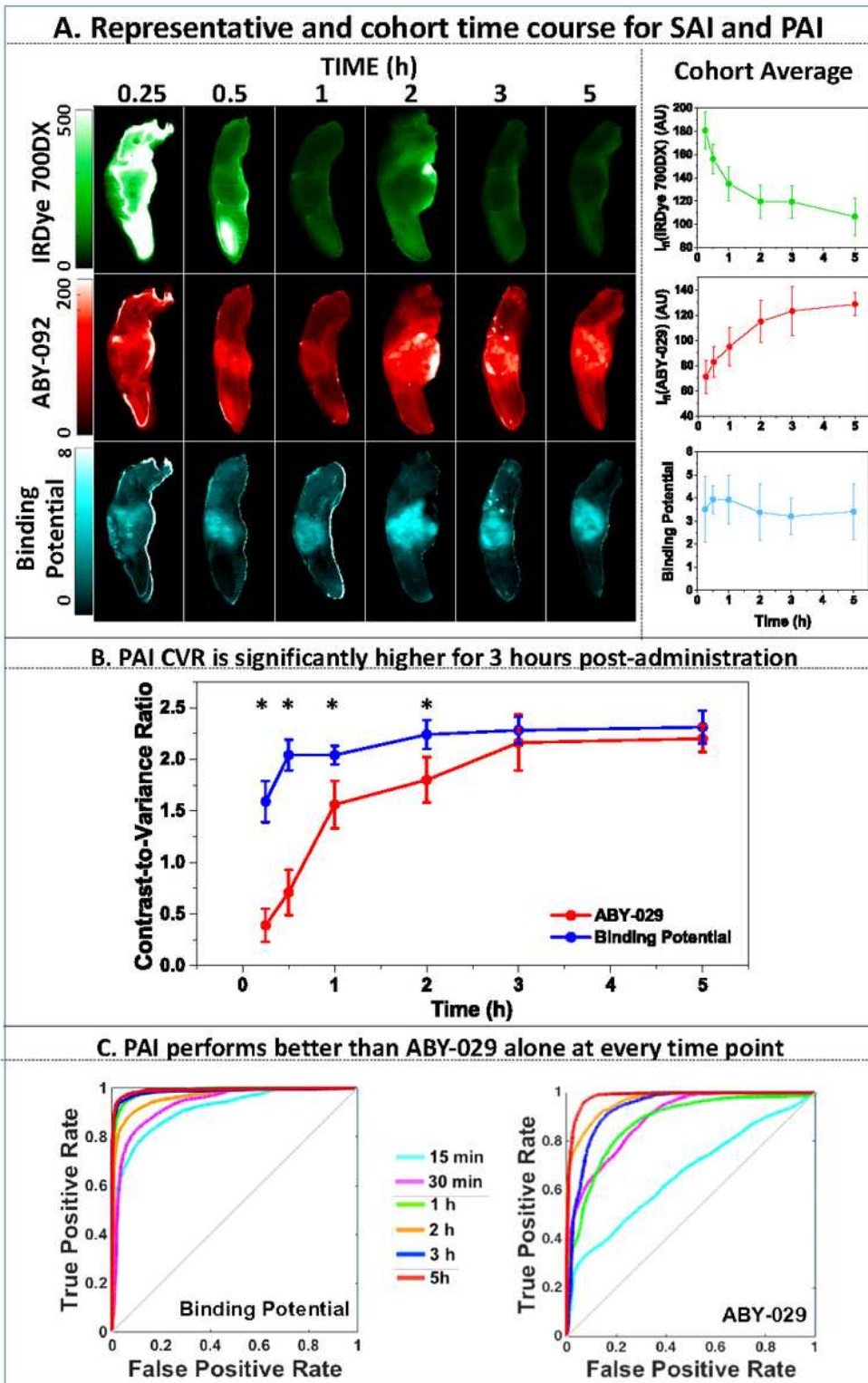


Figure 5

Comparison of administration-to-imaging time for PAI and SAI. (A) A representative image of the xenograft tongue tumors are shown for each SAI agent and PAI BP at each time point. The tumor cohort average for each time point is plotted to the right. BP is fairly constant over the 5-hour period, while fluorescence signal decreases for IRDye 700DX and increases for ABY-029 over time. (B) BP map determined CVR is significantly higher ($p < 0.05$) than that of ABY-029 over the first 2 hours after

administration, suggesting that BP provides a more stable tumor contrast measure. (C). ROC analysis indicates diagnostic abilities of both imaging methods improve over time; however, BP outperforms ABY-029 images, especially at short administration-to-imaging time points.

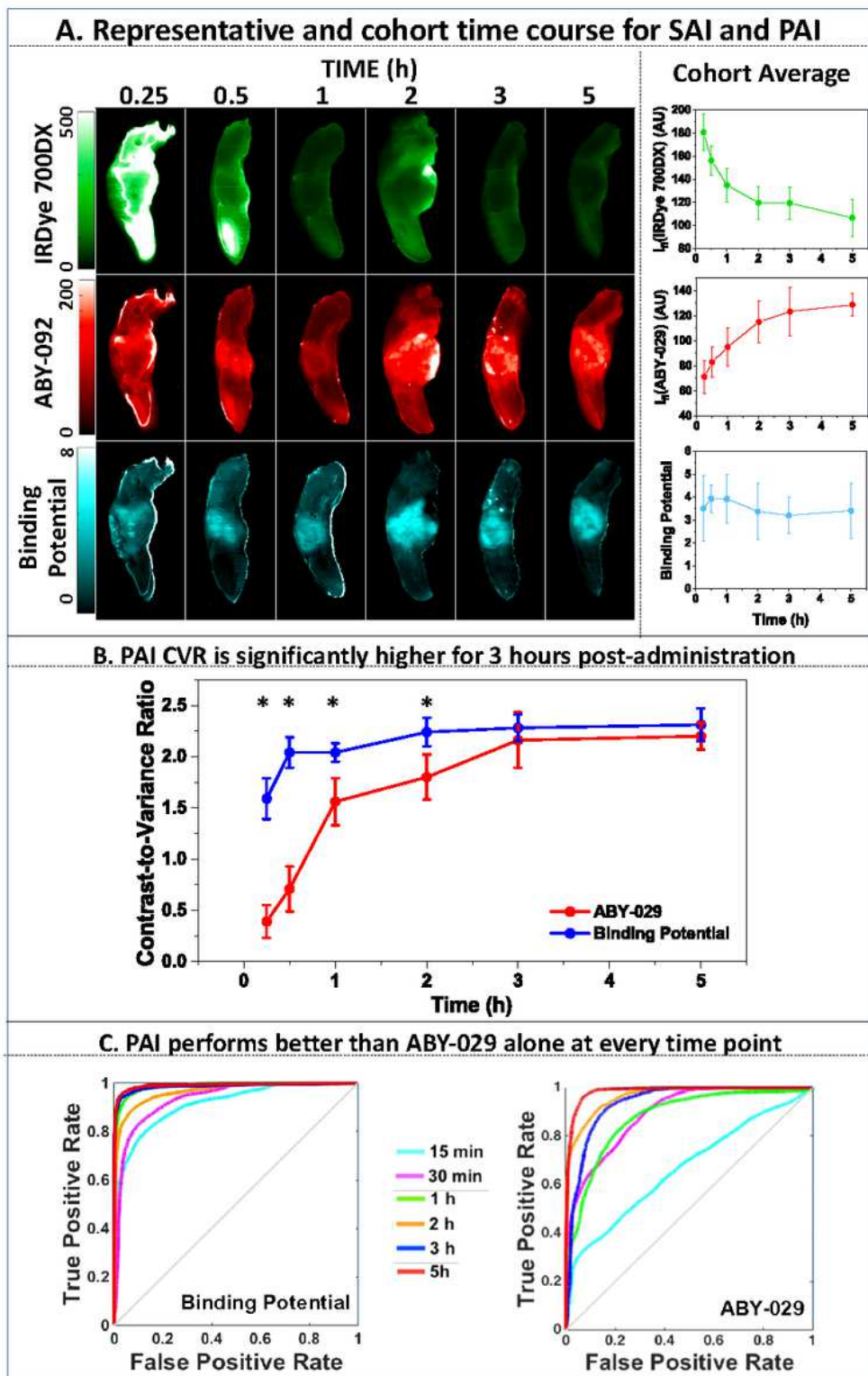


Figure 5

Comparison of administration-to-imaging time for PAI and SAI. (A) A representative image of the xenograft tongue tumors are shown for each SAI agent and PAI BP at each time point. The tumor cohort

average for each time point is plotted to the right. BP is fairly constant over the 5-hour period, while fluorescence signal decreases for IRDye 700DX and increases for ABY-029 over time. (B) BP map determined CVR is significantly higher ($p < 0.05$) than that of ABY-029 over the first 2 hours after administration, suggesting that BP provides a more stable tumor contrast measure. (C). ROC analysis indicates diagnostic abilities of both imaging methods improve over time; however, BP outperforms ABY-029 images, especially at short administration-to-imaging time points.

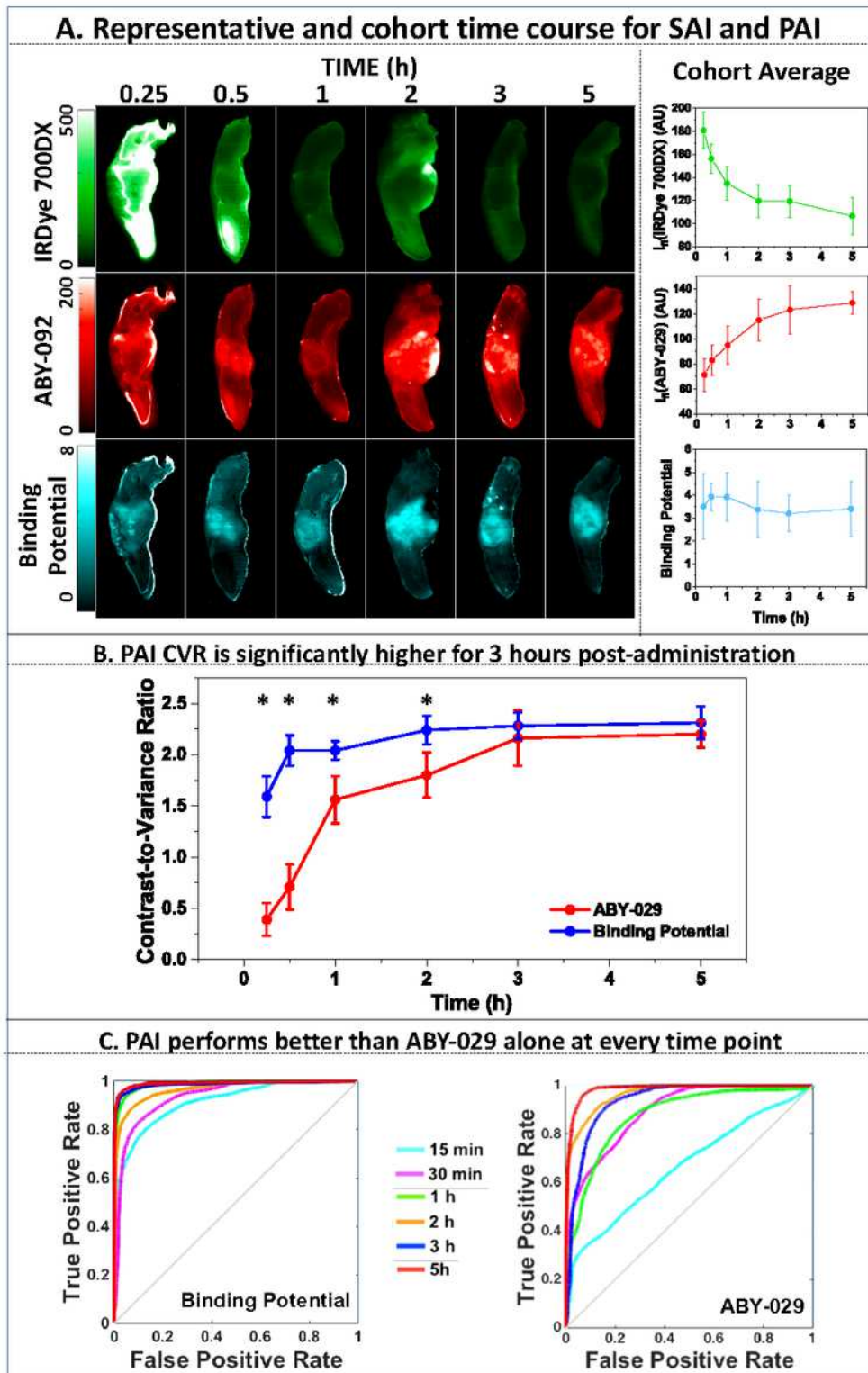


Figure 5

Comparison of administration-to-imaging time for PAI and SAI. (A) A representative image of the xenograft tongue tumors are shown for each SAI agent and PAI BP at each time point. The tumor cohort average for each time point is plotted to the right. BP is fairly constant over the 5-hour period, while fluorescence signal decreases for IRDye 700DX and increases for ABY-029 over time. (B) BP map determined CVR is significantly higher ($p < 0.05$) than that of ABY-029 over the first 2 hours after administration, suggesting that BP provides a more stable tumor con-trast measure. (C). ROC analysis indicates diagnostic abilities of both imaging methods improve over time; however, BP outperforms ABY-029 images, especially at short administration-to-imaging time points.

Supplementary Files

This is a list of supplementary files associated with this preprint. Click to download.

- [SupplementaryInformationJECCR.docx](#)
- [SupplementaryInformationJECCR.docx](#)
- [SupplementaryInformationJECCR.docx](#)